Modeling and Analysis of a Continuous Hydride Vapor Phase Epitaxy Manufacturing System for III-V Photovoltaics

by

Min Yao

A dissertation submitted in partial fulfillment of

the requirements for the degree of

Doctor of Philosophy

(Chemical Engineering)

at the

UNIVERSITY OF WISCONSIN-MADISON

2018

Date of final oral examination: 09/04/2018

The dissertation is approved by the following members of the Final Oral Committee:

James B. Rawlings, Professor, Chemical and Biological Engineering
Thomas F. Kuech, Professor, Chemical and Biological Engineering
Michael D. Graham, Professor, Chemical and Biological Engineering
Luke J. Mawst, Professor, Electrical and Computer Engineering
Victor M. Zavala, Associate Professor, Chemical and Biological Engineering

To Mom and Dad

ACKNOWLEDGMENTS

First and foremost, I would like to express my deepest gratitude to my advisers, Prof. James Rawlings and Prof. Thomas Kuech, for their invaluable guidance and continuous encouragement throughout my graduate career.

I would also like to extend my appreciation to Profs. Michael Graham, Luke Mawst and Victor Zavala for serving on my committee and commenting on this work.

Many thanks to Profs. Klingenberg and Graham as they provided illuminating discussions.

I would like to thank all the members from Rawlings and Kuech group for providing me generous help and delightful company. I am particularly thankful to Kevin Schulte as his help was instructive at the early stage of this research project. Thanks to Yingxin Guan and Junyan Miao for lending me their knowledge about the lab growth system and crystal growth. I also need to thank Hongyuk Kim from Mawst group for his input on device simulation.

I would like to acknowledge NSF (Grant Number: 1232618) for the financial support. I am also grateful to the university for providing convenient services and abundant resources. Thanks to the Center for High Throughput Computing (CHTC) for offering the computing resources and technical advice, and the department of Electrical and Computer Engineering for sharing the license of Silvaco software. Thanks to Prof. Feigl from the department of Geoscience for allowing us to share the license of COMSOL software.

I also want to thank the staff members in the department of Chemical and Biological Engineering for their professional assistance.

I would like to thank my friends in Madison for all the enjoyable moments we have shared.

Lastly, I would like to thank my parents and my brother for their love and caring, and my boyfriend, Shungang, for his infinite patience and understanding.

TABLE OF CONTENTS

LIST OF TABLES

LIST OF FIGURES

ABSTRACT

This work presents the modeling and analysis of a novel continuous hydride vapor phase epitaxy (HVPE) growth system that is designed for the efficient and controllable production of III-V multilayer heterostructures for photovoltaic application.

The proposed HVPE system comprises multiple deposition chambers isolated by separation zones. Substrates are transported by a moving belt through each deposition chamber where HVPE growth takes place under independent conditions. Such configuration eliminates the "latency" effect of reactant switching and thus enables the precise control of the interfacial composition.

To aid the process design, a reactor model is developed by updating the general transport model with moving mesh feature and incorporating a kinetic model for III-V HVPE growth established in this work. With this model, material properties such as film thickness, uniformity and composition can be predicted given the reactor geometry and process operating parameters.

The transport phenomena and the epilayer deposition in the growth system are studied through the reactor model. It is found that the gas-phase concentrations in the reactor show periodic variations over time while the deposition is occurring on moving substrates, which can be used to simplify the solution of the model. By investigating the influence of the design variables of the separation zone on the abruptness of the interfacial composition transition in heterostructures, it is found that a sharp interface can be produced

by decreasing the height of the separation zone even without a gas curtain. The model is further used to simulate the growth of a multilayer structure in solar cells and the feasibility of continuous growth in the proposed system is verified.

Finally, solar cell simulation is integrated to quantify the process performance in term of device efficiency. The influence of interface abruptness at the GaInP-GaAs heterojunction on the solar cell efficiency is investigated. It is found that the compositionally graded GaInAsP extra interlayer between GaInP-window and GaAs-emitter negatively affects the conversion efficiency of GaAs single junction solar cell. The solar cell efficiency decreases as the thickness of the transition layer increases. The result of this study confirms the effectiveness of the proposed continuous HVPE process for the growth of heterostructures.

1. INTRODUCTION

1.1 Motivation

III-V semiconductors and photovoltaics

Since their introduction to the photovoltaic application in the 1960s,[1] III–V compound semiconductor devices have replaced silicon-based solar cells as the major component of power supply system on spacecrafts, owing to their unparalleled efficiency,[2] light weight, and excellent radiation resistance. The extraordinary device performance is attributed to the properties of III-V materials. Advanced III-V photovoltaics are based on multilayer heterostructures; each layer is constituted by one kind of III–V compound semiconductors or related alloys. Group III-V compound semiconductors are formed by cations from group 13 (Al, Ga, In) and anions from group 15 (As, P, N, Sb, Bi). Most of the III-V semiconductors have a direct band gap[3,4] allowing effective light absorption, low electron effective mass, and high thermal conductivity.[5] Due to the chemical and crystallographic similarities, ternary and quaternary alloys with well-tailored lattice constants and bandgaps can be formed, integrated monolithically as heterostructures, and further combined as multijunctions, largely expanding the versatility of III-V materials and increasing the flexibility of device design.[6]

Fabrication methods and alternatives

Owing to the intensive research efforts on the pursuit of high efficiency, the current single-junction GaAs solar cell has reached the efficiency of 28.8 % under one sun, and

multijunction III-V has achieved 46 % at a concentration of 508 suns.[2]

Nonetheless, III-V photovoltaics are still only industrially viable in the area of space application,[7,8] multijunction concentrators,[9–12] and some niche fields, because of their prohibitively high fabrication cost. For the same area, the cost of producing a III-V solar cell is over 100 times higher than silicon.[13] The extra expenses mainly come from the cost of crystal substrates and epitaxial deposition process.[14]

The core structure of III-V solar cells is grown by a process called epitaxy. In a typical epitaxial growth, a single crystal substrate is placed in a vapor or liquid phase supersaturated with precursors, then this supersaturation drives the deposition of precursors upon the substrate that serves as the template of crystal structure, and the growth condition is finely tuned to control the structural registry between the deposited film and the substrate crystal.[15]

The cost of thick single crystal substrates (GaAs, InP) grown by bulk crystal growth systems (Czochralski, horizontal Bridgman, vertical Bridgman or vertical gradient freeze)[5] is the major impediment to the widespread use of III-V solar cells.[16] These substrates are essential for the epitaxial growth of high quality overlayers but not indispensable as a layer of the device for the solar energy conversion. Although there are considerable research efforts towards the heteroepitaxial growth of III-V semiconductors on inexpensive substrates such as silicon, this solution is not competitive because of limited cost reduction and inferior material quality.[17] In contrast, substrate removal and reuse is a far more

attractive approach.[14] Relevant techniques have been established over the last decades and proved to be adaptive to most growth technologies.[18]

The other principal impediment is the high cost related to the epitaxial deposition. While liquid phase epitaxy (LPE) was once widely adopted to produce III-V semiconductor devices,[19–21] nowadays the dominant growth technologies are metal organic vapor phase epitaxy (MOVPE) and molecular beam epitaxy (MBE).[22] These two techniques can produce a variety of high quality III-V multilayer heterostructures with precise control over composition, doping level and growth rate. However, neither of them is well suited to the manufacture of III-V devices for low-concentration terrestrial applications. The cost of MOVPE is high due to the large expense and low utilization of the precursors. MBE requires a high vacuum growth environment that limits the scalability and increases the costs of the equipment and operation. Furthermore, both of these processes suffer from the problem of low growth rate. The typical growth rates of MOVPE are 5-10 μm/h, and the growth rates for MBE are generally less than 3 μm/h. Such low rates of film deposition severely impair the mass production of III-V devices. Improving the throughput of epitaxial growth while utilizing low cost precursors is fundamental and essential to reduce the overall cost. But this strategy is hardly feasible by modifying the current MOVPE or MBE growth tools because of their process characteristics. A more cost-effective yet quality-competitive approach is needed to replace the mainstream growth methods.[23] A few promising candidates include hydride vapor-phase epitaxy (HVPE),[24] close-spaced vapor transport (CSVT),[25] and thin-film vapor-liquid-solid (TF-VLS) growth.[26]

HVPE method and challenges

As one of the prospective alternatives, hydride vapor phase epitaxy (HVPE) shares the most similarities with the MOVPE process,[27–29] allowing the integration of a new growth tool into the existing III-V PV production line with minimal alteration. HVPE is also a vapor-phase epitaxy method, but does not use expensive metalorganic III precursors and has higher utilization of V precursors. **Figure 1.1** illustrates a typical HVPE process for the epitaxial growth of GaAs layer. Group III atoms are transported into the growth system by flowing gaseous HCl over liquid Ga metal in a source zone. Arsine is introduced as group V precursor. Alloys with tunable composition such as $GaAs_yP_{1-y}$, $Ga_xIn_{1-x}P$, can be grown by adding an extra stream of PH_3 or flowing a stream of HCl through an extra source boat carrying In metal.

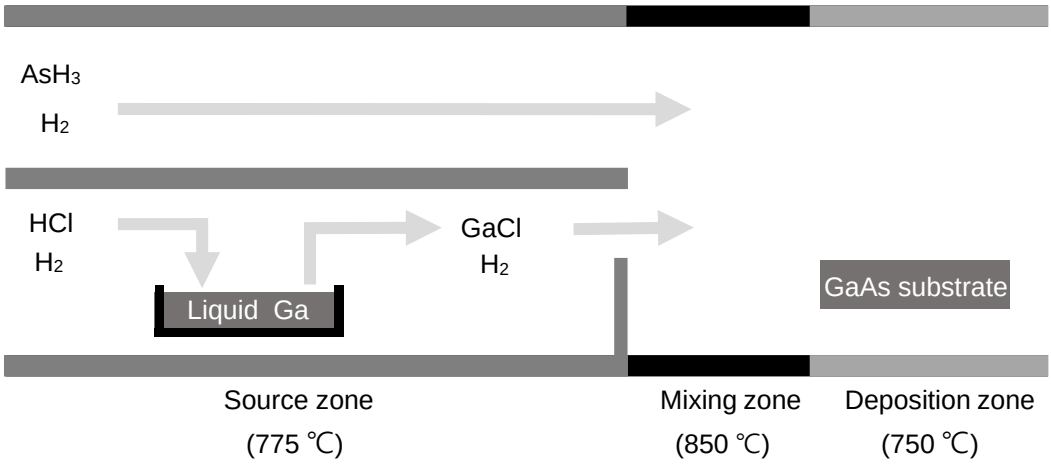

Figure 1.1 Schematic diagram of the HVPE process

The most distinctive advantage of HVPE is its high growth rate. The typical growth rates of HVPE are 30-50 μm/h, while under low pressure operation growth rates up to 300 μm/h have been reported.[30] However, there are also technical challenges limiting the HVPE production of III-V photovoltaics. Because the HVPE growth is typically operated near equilibrium and requires in-situ generation of III precursors at elevated temperatures, the growth of heterostructures with well-defined and abrupt interfaces is difficult to achieve. Several HVPE reactors were developed to address this issue but they were limited to the batch operation and difficult to scale up.[31–36] A more competitive strategy is to employ a multi-station growth configuration.[37–39] Recently a dual-chamber HVPE reactor was built in the National Renewable Energy Laboratory (NREL) as a prototype and has been used to grow a variety of advanced III-V solar cells.[40–44] The growth of multilayer heterostructures with abrupt interfaces is realized by mechanically transferring one substrate back and forth between two deposition chambers.[44] However, it is still essentially an intensified batch process. Some indispensable features of a high throughput continuous process, such as wafer-to-wafer interference and dynamic influence caused by the wafer transfer, cannot be studied through that physical system. To date, a controllable and fully continuous HVPE process for the manufacture of III-V solar cells is still absent.

1.2 Goals

Taking the aforementioned technical challenge as an opportunity, this work strives to develop a continuous hydride vapor phase epitaxy growth system capable of fabricating

III-V multilayer heterostructures with controllable material qualities for high-efficiency solar cells at higher throughput and lower per unit production cost compared to the conventional epitaxial growth tools. More specifically, we aim to

(1) propose the configuration of a prospective high-throughput HVPE growth system;

(2) develop a reaction-transport model to capture the growth characteristics and enable the reactor design;

(3) develop an approach to evaluate the growth process and material properties in term of device performance;

(4) prove the feasibility of this growth system for fabricating high quality III-V multilayer heterostructures in solar cells.

1.3 Dissertation Overview

This dissertation is organized as follows:

Chapter 1 introduces the background and motivation for this work.

Chapter 2 presents the operation and configuration of the continuous HVPE process proposed for the high throughput production of III-V multilayer heterostructures with controlled interfacial composition abruptness.

In Chapter 3, a transport-reaction model is formulated. This model includes a moving mesh to describe the dynamic reactor operation during growth and a semi-empirical kinetic model to relate the growth rate with gas-phase concentrations and growth temperature.

In Chapter 4, the modeling tool is applied to study the influence of moving substrates on the process characteristics and the design of the separation zone for the formation of abrupt heterointerface without operation interruption. The feasibility of the continuous HVPE process is examined and analyzed through simulating the growth of III-V multilayer heterostructures.

In Chapter 5, the approach of solar cell simulation is included to assess the quality of heterointerface in term of solar cell efficiency. A high-efficiency GaAs-based solar cell that is suitable to be manufactured through the continuous HVPE process is characterized and optimized through the numerical simulation.

Chapter 6 concludes this work and provides recommendations for future work.

2. CONTINUOUS HVPE REACTOR

2.1 Introduction

Hydride vapor phase epitaxy (HVPE) has been recognized as one of the most promising growth methods in the manufacture of low-cost III-V photovoltaics. The technical difficulty of forming abrupt interface between adjacent material layers has limited HVPE epitaxial growth of multilayer in batch or semi-batch processes.[34,45] In order to adapt the HVPE process for the mass production of III-V photovoltaics, we propose a continuous HVPE growth system potentially capable of growing multilayer heterostructures with controllable qualities at significantly greater throughput and lower per unit production cost compared to the conventional epitaxial growth tools.[46,47]

This proposed deposition system comprises multiple deposition chambers and interconnecting separation zones. Independent growth condition is established at steady state in each deposition zone to avoid the "latency" effect of gas switching on the formation of sharp interface. The placement of separation zone decouples the growth environment in different deposition zones and quenches the growth automatically to control the interfacial composition abruptness. This continuous HVPE growth system further includes at least one moving belt configured to continuously convey substrates through the linear cluster of the deposition and separation zones and a gas delivery assembly configured to deliver reactant gas mixtures to the growth system for deposition on the substrate via HVPE. The

configuration and operation of this continuous HVPE growth system will be further elaborated in the present chapter.

Although this type of reactor configuration and operation mode can be found in the conventional silicon industry and other general coating process, to the best of our knowledge, there is no prior literature applying this configuration in the HVPE process and the fabrication of III-V solar cells. There have been discussions in the literature[34,45] of the extension of existing semi-batch processing to a continuous growth system but no designs and design specifications have been presented.

2.2 Process Configuration

Figure 2.1 shows the block diagram of one prospective HVPE manufacturing system for continuous growth of III-V multilayer heterostructures. The entire growth system comprises the deposition assembly, gas delivery system, control system and auxiliary subsystems of wafer handling (loading/unloading), mechanical transport (moving belt), energy supply, exhaust gas treatment, and equipment cleaning.

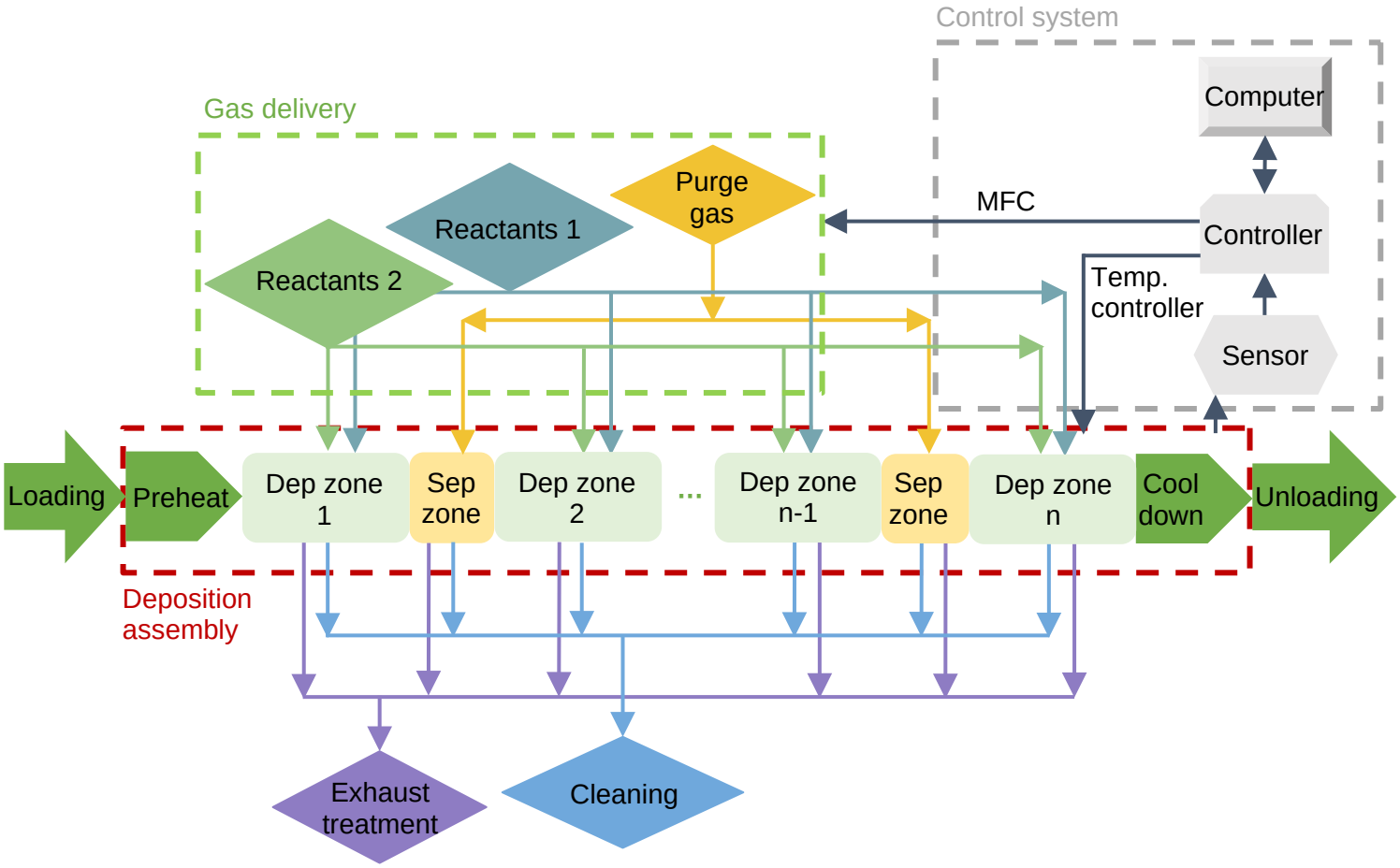

Figure 2.1 Prospective continuous HVPE growth system

Deposition assembly

The core of this continuous HVPE growth system is the deposition assembly that is composed of multiple deposition and separation chambers arranged alternately and one or multiple moving belts conveying wafers through all the chambers. Our work in this dissertation mainly centers on the deposition zones and separation zones, and the process characteristic adjusted by the operation of one moving belt.

There is one preheating zone located adjacent to the first deposition zone to heat up the loaded substrates and one cooling zone located at the end of the growth system to gradually cool the wafer to the room temperature prior to its unloading.

The precursors used in this HVPE system are AsH_3, PH_3, GaCl, and InCl. The group III chlorides are typically prepared in-situ in a source zone via reaction between HCl (carried by H_2) and liquid III metal held in a receptacle. In this high-throughput growth system, design of separated III source reactor is preferred due to large capacity and operation flexibility, but the details of the design are not included in this dissertation.

Gas delivery system

The gas delivery system locates at the upstream of the deposition system and provides specific gases to the designated locations on the deposition and separation chambers. The composition of the materials in the target multilayer heterostructure determines the types of gases delivered by the gas delivery system. To grow GaAs epilayers, the gas assembly delivers a stream of gaseous HCl (carried by H_2) into a source zone of liquid Ga to generate GaCl, a stream of AsH_3 and a carrier gas (e.g., H_2) into a mixing zone

where a homogeneous III and V mixture is prepared, and then promptly transported and delivered into the deposition zones. The gas delivery system also delivers the dopants to deposition zones, protective gases (e.g., AsH_3) to the separation, preheating, and cooling zones, cleaning gas (e.g., HCl) and purge gases (e.g., H_2, Ar, N_2) to the prescribed locations. The precise delivery of gases is crucial to the product quality and it requires the effective functioning of gas delivery system in conjunction with a control system.

Control system

The process parameters of the growth system, mainly temperatures, pressure, gas flowrates, and the speed of the moving belt, must be well controlled to guarantee the film quality and process reproducibility. A gas analyzer and in-situ real-time monitoring of epitaxial film growth may also be integrated.[48]

Energy supply

The HVPE reactor is operated under elevated temperatures. The temperatures are provided through external heaters and maintained at setpoint values in different locations of the growth system. For HVPE process, the source gases are preheated and mixed at higher temperatures than growth temperatures to avoid premature deposition.

Mechanical transport system

A mechanical transport system needs to be incorporated into the HVPE system for the operation of the moving belt. The speed of the moving belt is one key process parameter, which imposes stringent requirements on the sensitivity and reliability of the mechanical system.

Loading system

A mechanical loading system is also included to automatically load substrate into the growth chamber and unload product wafers off the growth system. This system may include at least two robot arms to transfer the wafers, a load lock chamber between the ambient and the preheating zone, and another load lock chamber between the cooling zone and the exterior.

Exhaust gas treatment

The outlets of the deposition and separation chambers are connected to an exhaust gas treatment system which typically consists of a sequence of cold trap, chemical trap, particle trap, and wet scrubber.[49] The effluent containing unreacted precursors and by-products is routed into the exhaust line, purified through each unit of the treatment system, and finally sent to the vent. The HVPE growth relies on the usage of highly toxic group V hydrides, AsH_3 and PH_3. Therefore, safety issues are of top priority. Besides the exhaust handling system, additional precautions such as toxic gas monitoring, alarming, and emergency shutdown should also be implemented.

Cleaning

The HVPE system further includes a cleaning assembly. As routine maintenance to ensure proper functioning of the growth system, the cleaning assembly is configured to introduce a selective etching gas, such as HCl, from the upstream gas delivery system into the growth chamber and remove the extraneous depositions on the moving belt and reactor walls.

2.3 Process Operation

The operation of the HVPE system is illustrated through the growth of multilayer heterostructures in a solar cell shown in **Figure 2.2**. The layers from n-GaAs buffer to the top p-GaAs cap layer can be grown in the proposed continuous HVPE system.

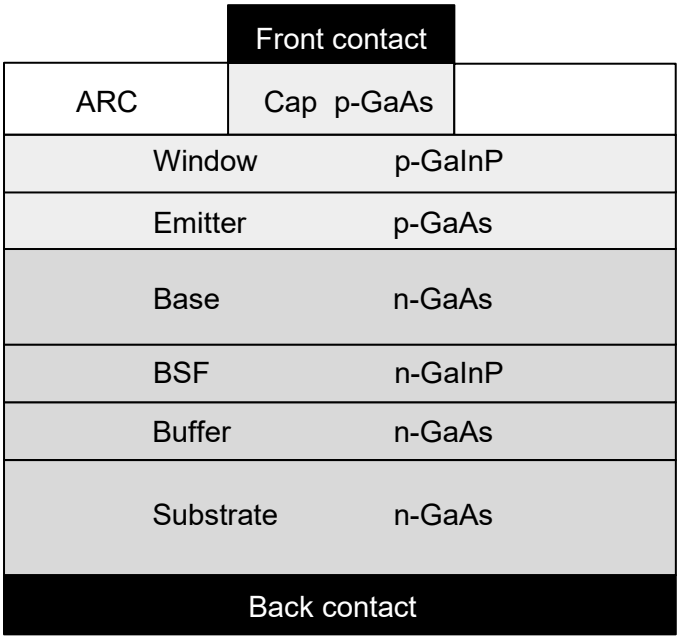

Figure 2.2 An example structure of multilayer GaAs-based solar cell

Figure 2.3(a) shows part of the continuous growth reactor for depositing the desired film. The entire reactor comprises six deposition zones that are separated from each other by separation zones. Substrates are transported linearly through each of these zones sequentially by a moving belt. In each of these deposition zones, one layer of the film with thickness and composition corresponding to the device structure is deposited. The

separation zone interrupts the growth of consecutive layers and guarantees the sharpness of the interfacial composition change.

For example, as illustrated in **Figure 2.3(b)**, the first deposition zone is designed to grow the first layer on top of the GaAs substrate, i.e., n-GaAs buffer layer. Through the top port of this deposition zone, a homogeneous mixture of reactants, i.e., GaCl, AsH_3 (and/or As_2, As_4), H_2, HCl, n-type dopants, is uniformly distributed downward over the surface of the multiple moving substrates. The deposition of GaAs takes place on each of the substrates present in the zone. The purity and doping level of the epilayer, or the composition of the solid, is controlled by the deposition temperature and gas-phase concentrations. The thickness of the epilayer is a function of the growth rate and the growth time. Since in this system, the growth time is predetermined by the speed of the moving belt and the length of the deposition zone, the growth rate needs to be well controlled to ensure that the thickness of the epilayer meets the specification. The growth rate is affected by the deposition temperature, the gas-phase composition and flow rate. Therefore, both the purity and thickness of the epilayer is guaranteed by a well-controlled gas-phase condition. This process requirement gives rise to the need to place a separation zone between the present zone and its succeeding deposition zone that is arranged to deposit another type of epilayer, GaInP. It is shown in **Figure 2.3** that the separation zone also has a top inlet through which a stream of purge gas, H_2 in this case, is delivered and forms a gas "curtain". Once the substrate is transported into the separation zone, the growth is quenched to avoid extra deposition. The separation zone also effectively prevents the cross-

contamination of gas-phase species in two adjacent deposition zones, thereby forming an abrupt solid composition transition from n-GaAs to n-GaInP.

Similarly, the other zones in this continuous growth system are operated to grow the remaining epilayers in the heterostructure (**Figure 2.2**).

Afterwards, the resultant heterostructure is processed into a solar device through conventional processing techniques. One typical procedure involves the deposition of front metal grid through photolithography and thermal evaporation, the selective removal of exposed cap layer from the active area, the deposition of rear-side metal contact, and the incorporation of a single-layer or double-layer antireflective coating (such as MgF_2/TiO_2).[50,51] If the target device is thin-film type and a sacrificial layer is grown, extra steps of selective etching and film transfer are required.

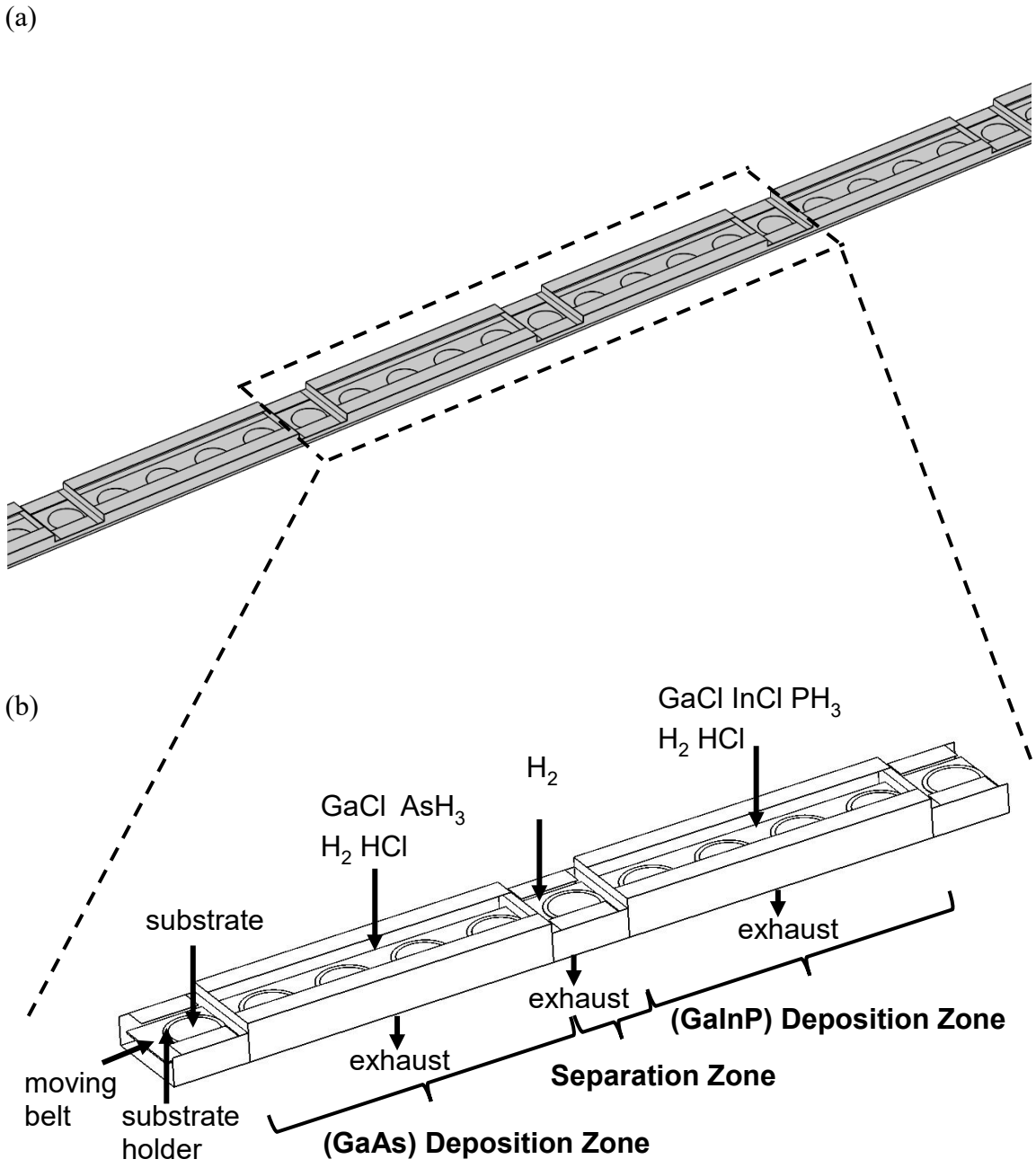

Figure 2.3 Sketch of the proposed HVPE reactor: (a) part of the continuous growth system, (b) details of two deposition zones and one separation zone

2.4 Process Highlights

For this continuous growth system, one distinguishing characteristic is that the deposition chambers and separation chambers are modular. Rather than vary zone sizes to achieve different growth requirements, we use optimized standard geometries of deposition and separation chambers and grow a variety of epilayers by flexibly combining multiple zones and adjusting the operating conditions. Based on this method, the scale-up of this growth system is readily accomplished. The HVPE growth system is especially suitable for the fabrication of single junction GaAs solar cell with GaInP window and BSF layers. But if other materials are involved in the target structure (such as AlAs sacrificial layer, Al-containing tunnel diode and wider bandgap window layer materials for GaInP subcell in multijunction solar cells), the modularized configuration of this HVPE process allows the flexibility of coupling with other growth tools, in particular the MOVPE reactors.

Another distinctive characteristic of this system is the design of the separation zone. An effective separation zone in a continuous moving belt reactor not only prevents the contamination from the neighboring deposition chamber, but also keeps the concentration of active reactants at the chosen values in each designated space. Applying purge gas can effectively prevent the transport of the reactants to the separation zone and the other deposition zones, but the flow rate of the purge gas needs to be well controlled. Otherwise, the excess purge gas interferes with the flow pattern in the deposition zones, dilutes the reactant concentration, and/or changes the ratio of V/III components. To minimize the effect of a separation zone on the growth rate, one approach is to speed up the transfer

process through the separation zone,[45] but this strategy is more appropriate for batch or semi-batch processes. For a continuous moving belt reactor, a constant speed of the belt through all of the chambers and zones is necessary; hence the approach we take is to maintain a growth environment that is as stable and as uniform as possible. The separation efficacy is mainly affected by the geometrical design of the zone, and the type[52] and flowrate of the purge gas. In this work, H_2 is chosen as the purge gas for simplicity and the effects of the other two factors on the interface quality are studied.

2.5 Conclusions

In this chapter, a fully continuous moving belt HVPE deposition system that targets the low-cost growth of III-V heterostructures is presented. The growth system is designed to realize the advantages of hydride VPE method in the rapid growth of III-V compounds and overcome the technical challenge in the precise control of heterojunction formation by HVPE through process design. We are expecting this design can aid the high throughput production of III-V multilayer heterostructures with controlled quality and potentially promote the widespread adoption of III-V photovoltaics in terrestrial applications. In the following chapters, computational modeling is used to investigate the major design and operating strategies introduced here.

3. MODEL FORMULATION

3.1 Introduction

In this previous chapter, we have presented a HVPE process for the high throughput growth of III-V heterostructure solar cells. Because of the complexity and cost of the process, it is intractable to design such a process exclusively via trial-and-error methods. Instead, we employ a model-based design approach that is more flexible and cost-effective.

In contrast to the considerable publications on the modeling of MOVPE growth systems,[53–58] computational studies of HVPE process are much fewer. By reviewing relevant literatures, we can roughly divide them into two categories: (1) HVPE chemistry modeling studies, focusing on the complex reaction mechanism in the gas phase and at the surface. There are two models of this kind developed by Cadoret et al.[59,60] and Korec et al.[61,62] respectively for the HVPE growth of GaAs. It is worth mentioning that Seifert has carried out semi-empirical quantum chemical calculations[63] to study the chorine desorption by molecular hydrogen, which is the rate-limiting surface process proposed in Cadoret and Korec's growth models. Besides these two theoretical growth models, there are also semi-empirical growth rate models developed which rely on the experimental data[64] to estimate unknown parameters in the rate law derived from specific mechanism with simplications.[65,66] Various growth models have also been presented for HVPE of III-V alloys, such as $Ga_xIn_{1-x}As$,[67,68] $InAs_{1-x}P_x$,[69] $Ga_xIn_{1-x}As_yP_{1-y,}$[70,71] and simulation results are claimed to be consistent with experiment data; (2) HVPE reactor modeling studies, aiming

at elucidating the effects of fluid transport or heat transfer on film growth rate and uniformity within the constraints of process operating conditions and reactor geometry factors, usually in combination with rather simple or lumped chemistry. The modeling of transport phenomena in VPE reactors has been studied and reviewed extensively in the literature.[72–74] The availability of many commercial Computational Fluid Dynamics (CFD) packages (e.g., Fluent,[75] COMSOL Multiphysics,[76] CFD-ACE+[77]) and the increase in high-performance computing capability greatly facilitate the work of designing and optimizing the operating conditions as well as the reactor configurations for CVD process. Most CFD modeling work about the HVPE process is associated with the growth of GaN.[78–82] This method is also adopted to aid the design of dual chamber HVPE growth system for III-V solar cells in NREL.[52,83]

In order to model the HVPE deposition of III-V multilayer heterostructure in the proposed continuous reactor, in this chapter, we update the classic model framework, which comprises conservation equations of mass, momentum, energy and species, with new features that are unique to the III-V HVPE growth system and continuous configuration. This model is expected to be an effective tool to predict the quality of grown films provided the operating and geometrical conditions and to optimize the reactor design given material specifications.

3.2 Assumptions

This HVPE process is operated at near atmospheric pressure and in the laminar flow regime. The gas mixture is regarded as an ideal, incompressible, and Newtonian continuum.

Dilute mixture approximation

Since the concentrations of species in HVPE systems are much lower than that of the carrier gas, the dilute mixture approximation is employed.[84] According to this approach, the properties of the gas mixture are approximated by those of the carrier gas, which simplifies the evaluation of the transport properties.

Isothermal operation

Different from MOVPE, HVPE is usually conducted in hot-wall reactors. Although the modular configuration of this deposition system allows the feasibility of operating deposition zones in different temperatures, it is preferable to operate the entire HVPE deposition assembly at one temperature to avoid thermal shock of the substrate wafer during the transport through the system. Therefore, the isothermal assumption is made in this work and the conservation equation for energy is excluded from the governing equations of this model.

Moving mesh

To improve the accuracy of this model, a moving mesh is adopted to solve the transient transport and growth models during the movement of the belt and the substrates.

The transport equations for fluid flow and mass transfer in the Eulerian forms are updated to the moving coordinates.[85,86]

3.3 Transport Model

3.3.1 Governing equations

$$\rho\nabla\cdot\mathbf{v}=0 \tag{3.1}$$

$$\rho\frac{\partial\mathbf{v}}{\partial t}+\rho\left(\mathbf{v_c}\cdot\nabla\right)\mathbf{v}=\nabla\cdot\left[-p\mathbf{I}+\mu\left(\nabla\mathbf{v}+\left(\nabla\mathbf{v}\right)^{T}\right)\right]+\rho\mathbf{g} \tag{3.2}$$

$$\frac{\partial c_i}{\partial t}+\mathbf{v_c}\cdot\nabla c_i=\nabla\cdot\left(D_{ic}\nabla c_i\right)+R_{g,i} \tag{3.3}$$

$$\mathbf{v_c}=\mathbf{v}-\hat{\mathbf{v}} \tag{3.4}$$

where $\mathbf{v}$, $\hat{\mathbf{v}}$, and $\mathbf{v_c}$ are material velocity, mesh velocity, and convective velocity, respectively. Based on the dilute mixture assumption, the density and viscosity of gas mixture are given as those of the carrier gas, H_2. The density of H_2 is obtained from the ideal gas law, $\rho=\frac{pM_{\mathrm{H_2}}}{R_{\mathrm{const}}T}$. **Equation 3.3** describes the unsteady diffusion-convection of each dilute species i, where c_i is the concentration of each dilute gas-phase species, i.e., i=GaCl, AsH_3, InCl, PH_3, HCl and $i \neq H_2$. The variable of D_{ic} denotes the binary diffusion coefficient of each species i in the carrier gas. The variable of $R_{g,i}$ is the production rate of species i due to the gas-phase reactions. Additionally, a model equation describing the mesh velocity $\hat{\mathbf{v}}$ is required. This model smoothly deforms the interior mesh that is

bounded by the prescribed $\hat{\mathbf{v}}$ or position. A Laplacian smoothing algorithm is selected for this work.[87,88] In this smoothing procedure, the mesh deforms while the number of elements remains unchanged. Therefore, remeshing the domain is required once the distortion becomes significant.

3.3.2 Initial and boundary conditions

The initial and boundary conditions are determined by the specific operation under investigation. In this work, the growth during the steady operation is of more interest rather than the start-up of the reactor. Therefore, the model is solved first in a stationary mode, i.e., the transient terms, $\frac{\partial \mathbf{v}}{\partial t}$ and $\frac{\partial c_i}{\partial t}$, and the mesh velocity, $\hat{\mathbf{v}}$, in governing **Equations 3.2-3.4** are set to zero; the solution of the static mode is then used as the initial condition for the time-dependent mode that takes the movement of the substrate and belt into account. **Figure 3.1** illustrates the boundary conditions of the proposed model.

Inlet

A homogeneous preheated mixture of precursors and carrier gas is uniformly distributed from the top inlet of the deposition zone. At the inlet of the separation zone, depending on the operating condition, either an inflow (H_2 in this study) or a wall condition is assigned.

$$\mathbf{v} = v_{in}\mathbf{n} \qquad\qquad c_i = c_{i,in}$$

where subscript in denotes the inflow, **n** means the direction of inflow is normal to the inlet, i.e., $v_x = v_y = 0$, $v_z = v_{in}$. The inlet concentration of each dilute gas-phase species

is given as $c_{i,in}$, i = GaCl, AsH_3, InCl, PH_3, HCl.

Outlet

The pressure condition is prescribed at the bottom exit to suppress the flow back into the growth system. It is assumed that convection dominates the outflow, hence there is no diffusion of species across the exit boundary.

$$[-p\mathbf{I} + \mu(\nabla\mathbf{v} + (\nabla\mathbf{v})^{\mathrm{T}})]\mathbf{n} = -\hat{p}_0\mathbf{n},\ \hat{p}_0 \leq p_0 \qquad \mathbf{n} \cdot D_i\nabla c_i = 0$$

Substrate

For thin films, the effect of the film growth and the substrate thickness on the flow velocity are neglected. The flow velocity is equal to the speed of the moving belt because a no-slip condition applies on the substrate surface as well as between the substrate and the belt. The flux of species i on the substrate is balanced by the production rate of this species due to surface reactions, $R_{s,i}$. A kinetic model is required to describe the rates of surface reactions given the growth conditions.

$$v_x = v_b \qquad \mathbf{n} \cdot \nabla(D_i c_i) = R_{s,i} \tag{3.5}$$

Belt

The speed of the moving belt, v_b, determines the throughput of the continuous growth system. Depending on the form of the belt, models of different complexity can be included. For example, the permeability of the belt could affect the distribution of gas flow and species transport. If a perforated belt is used, the gas velocity in the z direction is prescribed a non-zero value, v_l. For an impermeable belt, $v_l = 0$ and there is no flux of species into the inert belt.

$v_x = v_b$ $v_z = v_l$ $\mathbf{n} \cdot \nabla(D_i c_i) = v_z \cdot c_i$

Walls

It is generally assumed that gas cannot penetrate or slip on the reactor walls. Parasitic deposition on the reactor walls is excluded. The following conditions are used to describe the static and non-reacting reactor walls.

$\mathbf{v} = 0$ $\mathbf{n} \cdot \nabla c_{\mathrm{i}} = 0$

Moving boundaries

For rigid reactor walls and open boundaries such as inlet and outlet, the mesh is fixed, i.e., $\hat{\mathbf{v}} = 0$. In cases where the substrates and belt move at a speed of v_b, the mesh also moves correspondingly, i.e., $\hat{v}_x = v_b$.

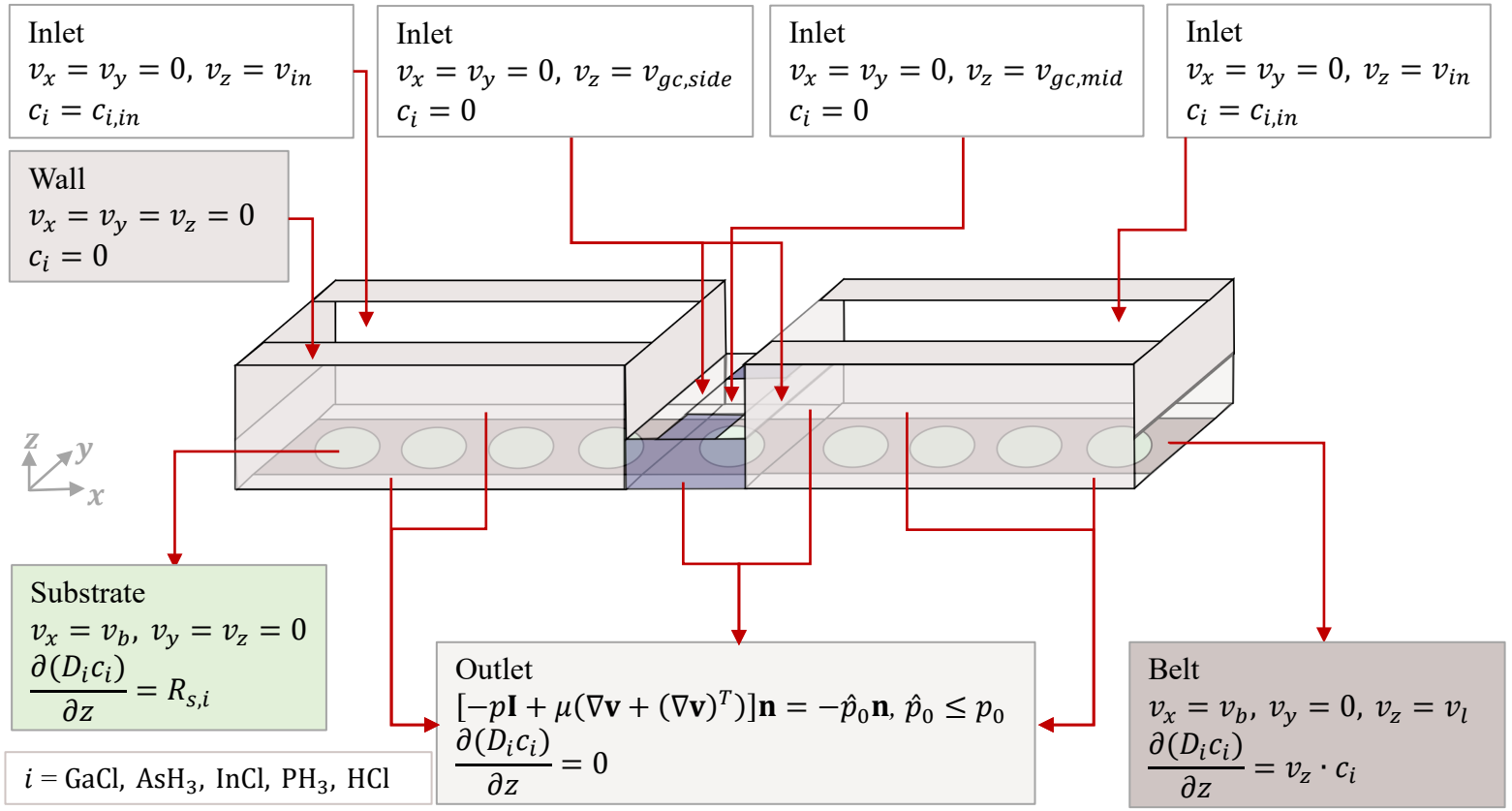

Figure 3.1 Boundary conditions of the reactor model (not drawn to scale) at one specific time step

3.3.3 Transport properties

Diffusivity

The Fick's law diffusion model with binary diffusion coefficient of each species in carrier gas, H_2, is used for the calculations simplified with the dilute mixture assumption. The dependence of diffusivities on gas composition is eliminated in this simplification.

In our system, which involves 6 species: H_2 (carrier), AsH_3, GaCl, InCl, PH_3, HCl, five D_{ic} should be provided. In this study, D_{ic} is calculated by Gilliland's equation:[89]

$$D_{ic} = 4.3 \times 10^{-3} \frac{T^{3/2}(1/M_i + 1/M_c)^{1/2}}{p(V_i^{1/3} + V_c^{1/3})^2}$$

Here,

D_{ic}: binary diffusion coefficients of species *i* in carrier, cm^2/s

T: temperature, K

M_i, M_c: molecular weights of species *i* and carrier, g/mol

V_i, V_c: molecular volume in the liquid phase at the boiling point of species *i* and carrier, cm^3

p: total pressure, approximately 1atm in our system.

3.4 Kinetic Model

3.4.1 Mechanism and formulation

Nominally only the reaction rate expressions of HVPE of GaAs and GaInP are needed for modeling the deposition of these layers (**Figure 2.2**). But since the separation

zone is not perfect, there is "cross-contamination" of gas species between two adjacent growth chambers. Therefore, in the general case, there are four overall growth reactions (**Equations 3.6-3.9**).

$$GaCl + \frac{1}{4}As_4 + \frac{1}{2}H_2 \rightleftarrows GaAs + HCl \quad (3.6)$$

$$InCl + \frac{1}{4}As_4 + \frac{1}{2}H_2 \rightleftarrows InAs + HCl \quad (3.7)$$

$$GaCl + \frac{1}{4}P_4 + \frac{1}{2}H_2 \rightleftarrows GaP + HCl \quad (3.8)$$

$$InCl + \frac{1}{4}P_4 + \frac{1}{2}H_2 \rightleftarrows InP + HCl \quad (3.9)$$

The deposited material can be a binary semiconductor such as GaAs, a ternary semiconductor such as GaInP that is regarded as an alloy of GaP and InP, or any other alloy denoted by the general form of $Ga_xIn_{1-x}As_yP_{1-y}(0 \leq x \leq 1, 0 \leq y \leq 1)$.

For the actual HVPE growth, the group V precursor is usually a mixture of As_4, As_2, and AsH_3 (for the growth chamber of GaAs) or a mixture of P_4, P_2, and PH_3 (for the growth chamber of $Ga_{0.51}In_{0.49}P$), depending on the source gas and operating conditions. The source gas is arsine or phosphine in a gas cylinder, from which these hydrides are transported separately into heated source zones and decomposed partially or completely (**Equations 3.10-3.13**). The literature reports that different forms of V precursors have different abundance and reactivities in semiconductor growth,[90,91] so it is possible to adjust

the process performance by maintaining a desirable type of precursor at a relatively high ratio.[92]

$$AsH_3 \xrightleftharpoons{K_1} \frac{1}{2}As_2 + \frac{3}{2}H_2 \qquad K_1 = \frac{{c_{As_2}}^{1/2}{c_{H_2}}^{3/2}}{c_{AsH_3}} \tag{3.10}$$

$$As_4 \xrightleftharpoons{K_2} 2As_2 \qquad K_2 = \frac{{c_{As_2}}^{2}}{c_{As_4}} \tag{3.11}$$

$$PH_3 \xrightleftharpoons{K_3} \frac{1}{2}P_2 + \frac{3}{2}H_2 \qquad K_3 = \frac{{c_{P_2}}^{1/2}{c_{H_2}}^{3/2}}{c_{PH_3}} \tag{3.12}$$

$$P_4 \xrightleftharpoons{K_4} 2P_2 \qquad K_4 = \frac{{c_{P_2}}^{2}}{c_{P_4}} \tag{3.13}$$

By contrast, the group III precursor, i.e., GaCl or InCl, is typically generated through reactions between liquid Ga or In metal and gaseous HCl in another source zone with a high conversion ratio (**Equations 3.14-3.15**). We assume complete conversion is achieved through a well-designed source zone, hence the flow rate of III precursor into the deposition zone can be determined by the flow rate of HCl flowing through Ga or In source zone.

$$Ga + HCl \longrightarrow GaCl + \frac{1}{2}H_2 \tag{3.14}$$

$$In + HCl \longrightarrow InCl + \frac{1}{2}H_2 \tag{3.15}$$

To relate the growth rates of solids with the gas-phase conditions, a semi-empirical mechanism for surface reactions is proposed (**Equations 3.16-3.26**). This postulated mechanism takes the surface adsorption, reaction and desorption into account.

1: $\mathrm{As_2} + 2* \overset{K_5}{\rightleftarrows} 2\mathrm{As}*$ $$K_5 = \frac{[\mathrm{As}\,*]^2}{c_{\mathrm{As_2}}[*]^2} \quad (3.16)$$

2: $\mathrm{P_2} + 2* \overset{K_6}{\rightleftarrows} 2\mathrm{P}*$ $$K_6 = \frac{[\mathrm{P}\,*]^2}{c_{\mathrm{P_2}}[*]^2} \quad (3.17)$$

3: $\mathrm{As}* + \mathrm{GaCl} \overset{K_7}{\rightleftarrows} \mathrm{AsGaCl}*$ $$K_7 = \frac{[\mathrm{AsGaCl}\,*]}{[\mathrm{As}\,*]c_{\mathrm{GaCl}}} \quad (3.18)$$

4: $\mathrm{As}* + \mathrm{InCl} \overset{K_8}{\rightleftarrows} \mathrm{AsInCl}*$ $$K_8 = \frac{[\mathrm{AsInCl}\,*]}{[\mathrm{As}\,*]c_{\mathrm{InCl}}} \quad (3.19)$$

5: $\mathrm{P}* + \mathrm{GaCl} \overset{K_9}{\rightleftarrows} \mathrm{PGaCl}*$ $$K_9 = \frac{[\mathrm{PGaCl}\,*]}{[\mathrm{P}\,*]c_{\mathrm{GaCl}}} \quad (3.20)$$

6: $\mathrm{P}* + \mathrm{InCl} \overset{K_{10}}{\rightleftarrows} \mathrm{PInCl}*$ $$K_{10} = \frac{[\mathrm{PInCl}\,*]}{[\mathrm{P}\,*]c_{\mathrm{InCl}}} \quad (3.21)$$

7: $\mathrm{AsGaCl}* + \mathrm{H_2} \xrightarrow{k_{11}} \mathrm{GaAs} + \mathrm{HCl} + \mathrm{H} + *$ $$r_{11} = k_{11}[\mathrm{AsGaCl}\,*]c_{\mathrm{H_2}} \quad (3.22)$$

8: $\mathrm{AsInCl}* + \mathrm{H_2} \xrightarrow{k_{12}} \mathrm{InAs} + \mathrm{HCl} + \mathrm{H} + *$ $$r_{12} = k_{12}[\mathrm{AsInCl}\,*]c_{\mathrm{H_2}} \quad (3.23)$$

9: $\mathrm{PGaCl}* + \mathrm{H_2} \xrightarrow{k_{13}} \mathrm{GaP} + \mathrm{HCl} + \mathrm{H} + *$ $$r_{13} = k_{13}[\mathrm{PGaCl}\,*]c_{\mathrm{H_2}} \quad (3.24)$$

10: $\mathrm{PInCl}* + \mathrm{H_2} \xrightarrow{k_{14}} \mathrm{InP} + \mathrm{HCl} + \mathrm{H} + *$ $$r_{14} = k_{14}[\mathrm{PInCl}\,*]c_{\mathrm{H_2}} \quad (3.25)$$

11: $2\mathrm{H} \overset{k_{15}}{\rightleftarrows} \mathrm{H_2}$ $$K_{15} = \frac{c_{\mathrm{H_2}}}{c_{\mathrm{H}}{}^2} \quad (3.26)$$

where * is a free surface site, [*] is the surface concentration of the free surface site *, i* denotes an adsorbed species, [i*] is the surface concentration of the adsorbed species i*.

Since the deposition reactions are usually operated under locally non-etching conditions, the HCl etching steps are neglected. It is assumed that reactive desorption of

chlorine by H_2, **Steps 7-10**, is rate-limiting and all other steps are at equilibrium. The rates of these steps are given as **Equations 3.22-3.25**. The surface terms in these equations are eliminated by using the equilibrium relations (**Equations 3.16-3.21**, **3.26**).

$$r_{11} = k_{11}K_7 c_{\mathrm{GaCl}}\sqrt{K_5 c_{\mathrm{As_2}}}[*]c_{\mathrm{H_2}} \tag{3.27}$$

$$r_{12} = k_{12}K_8 c_{\mathrm{InCl}}\sqrt{K_5 c_{\mathrm{As_2}}}[*]c_{\mathrm{H_2}} \tag{3.28}$$

$$r_{13} = k_{13}K_9 c_{\mathrm{GaCl}}\sqrt{K_6 c_{\mathrm{P_2}}}[*]c_{\mathrm{H_2}} \tag{3.29}$$

$$r_{14} = k_{14}K_{10} c_{\mathrm{InCl}}\sqrt{K_6 c_{\mathrm{P_2}}}[*]c_{\mathrm{H_2}} \tag{3.30}$$

Then a site balance is carried out.

$$\Gamma = [*] + [\mathrm{As}*] + [\mathrm{P}*] + [\mathrm{AsGaCl}*] + [\mathrm{AsInCl}*] + [\mathrm{PGaCl}*] + [\mathrm{PInCl}*] \tag{3.31}$$

where Γ is the total concentration of surface sites.

From **Equations 3.16-3.21** and **Equation 3.31**, the surface concentration of the free sites can be represented as

$$[*] = \frac{\Gamma}{1+\sqrt{K_5 c_{\mathrm{As_2}}}(1+K_7 c_{\mathrm{GaCl}}+\mathrm{K_8} c_{\mathrm{InCl}})+\sqrt{K_6 c_{\mathrm{P_2}}}(1+K_9 c_{\mathrm{GaCl}}+K_{10} c_{\mathrm{InCl}})} \tag{3.32}$$

Substituting **Equation 3.32** into **Equations 3.27-3.30** provides the growth rate expressions for the solid species.

In our simulations, we assume the V precursor entering the deposition zones is AsH_3 or PH_3 and the gas-phase reactions (**Equations 3.10-3.13**) are at equilibrium. The expressions for the growth rates of each solid species are given as follows:

$$R_{\mathrm{GaAs}} = \frac{N_1 c_{\mathrm{AsH3}} c_{\mathrm{GaCl}} c_{\mathrm{H2}}}{1+D_1 c_{\mathrm{AsH3}}+D_2 c_{\mathrm{AsH3}} c_{\mathrm{GaCl}}+D_3 c_{\mathrm{AsH3}} c_{\mathrm{InCl}}+D_4 c_{\mathrm{PH3}}+D_5 c_{\mathrm{PH3}} c_{\mathrm{GaCl}}+D_6 c_{\mathrm{PH3}} c_{\mathrm{InCl}}} \tag{3.33}$$

$$R_{\mathrm{InAs}} = \frac{N_2\, c_{\mathrm{AsH3}} c_{\mathrm{InCl}} c_{\mathrm{H2}}}{1+D_1 c_{\mathrm{AsH3}}+D_2 c_{\mathrm{AsH3}} c_{\mathrm{GaCl}}+D_3 c_{\mathrm{AsH3}} c_{\mathrm{InCl}}+D_4 c_{\mathrm{PH3}}+D_5 c_{\mathrm{PH3}} c_{\mathrm{GaCl}}+D_6 c_{\mathrm{PH3}} c_{\mathrm{InCl}}} \quad (3.34)$$

$$R_{\mathrm{GaP}} = \frac{N_3 c_{\mathrm{PH3}} c_{\mathrm{GaCl}} c_{\mathrm{H2}}}{1+D_1 c_{\mathrm{AsH3}}+D_2 c_{\mathrm{AsH3}} c_{\mathrm{GaCl}}+D_3 c_{\mathrm{AsH3}} c_{\mathrm{InCl}}+D_4 c_{\mathrm{PH3}}+D_5 c_{\mathrm{PH3}} c_{\mathrm{GaCl}}+D_6 c_{\mathrm{PH3}} c_{\mathrm{InCl}}} \quad (3.35)$$

$$R_{\mathrm{InP}} = \frac{N_4 c_{\mathrm{PH3}} c_{\mathrm{InCl}} c_{\mathrm{H2}}}{1+D_1 c_{\mathrm{AsH3}}+D_2 c_{\mathrm{AsH3}} c_{\mathrm{GaCl}}+D_3 c_{\mathrm{AsH3}} c_{\mathrm{InCl}}+D_4 c_{\mathrm{PH3}}+D_5 c_{\mathrm{PH3}} c_{\mathrm{GaCl}}+D_6 c_{\mathrm{PH3}} c_{\mathrm{InCl}}} \quad (3.36)$$

For simplicity, the rate constants and equilibrium constants are lumped into the terms of N_1-N_4 and D_1-D_6. The correspondence is shown in **Table 3.1**.

These coefficients are assumed to be in the Arrhenius form and can be estimated from experimental growth data. The term of $R_{s,i}$ (i=GaCl, AsH_3, InCl, PH_3, HCl, H_2) in the boundary condition on the substrate (**Equation 3.5**), can then be expressed as a function of gas species concentrations through **Equations 3.33-3.36**. For example, $R_{s,\mathrm{GaCl}} = -R_{\mathrm{GaAs}} - R_{\mathrm{GaP}}$, $R_{s,\mathrm{HCl}} = R_{\mathrm{GaAs}} + R_{\mathrm{InAs}} + R_{\mathrm{GaP}} + R_{\mathrm{InP}}$, etc.

Table 3.1 Coefficients of the kinetic model

Lumped parameter	Expression	Lumped parameter	Expression
N_1	$\Gamma k_{11} K_7 \sqrt{K_5 K_1}$	N_3	$\Gamma k_{13} K_9 \sqrt{K_6 K_3}$
N_2	$\Gamma k_{12} K_8 \sqrt{K_5 K_1}$	N_4	$\Gamma k_{14} K_{10} \sqrt{K_6 K_3}$
D_1	$\sqrt{K_5 K_1}$	D_4	$\sqrt{K_6 K_3}$
D_2	$\sqrt{K_5 K_1} K_7$	D_5	$\sqrt{K_6 K_3} K_9$
D_3	$\sqrt{K_5 K_1} K_8$	D_6	$\sqrt{K_6 K_3} K_{10}$

3.4.2 Parameter estimation

Because of the unavailability of sufficient kinetic growth data for III-V semiconductors (e.g., GaInP) except GaAs, these unknown parameters have to be inferred from a variety of data sources; therefore, the uncertainties of the parameters in this model may be significant.

There are relatively extensive experimental growth rate data from the study by Shaw[64] for the HVPE growth of GaAs. For each run of experiments in that study, the weight of substrate is continuously measured by a microbalance while the temperature is slowly varied at a fixed gas-phase composition, thereby providing the variation of deposition rate versus the deposition temperature. The partial pressure of GaCl or As_4 is then adjusted to

a new value and the measurement with temperature variation is repeated. The growth rate of GaAs is given by

$$R_{\mathrm{GaAs}} = \frac{x_1 \exp(\frac{x_2}{T}) {p_{\mathrm{As_4}}}^{\frac{1}{4}} p_{\mathrm{GaCl}}\, p_{\mathrm{H_2}}}{1 + x_3 \exp(\frac{x_4}{T}) {p_{\mathrm{As_4}}}^{\frac{1}{4}} + x_5 \exp(\frac{x_6}{T}) {p_{\mathrm{As_4}}}^{\frac{1}{4}} p_{\mathrm{GaCl}}} \tag{3.37}$$

where $p_{\mathrm{As_4}}$, p_{GaCl}, and $p_{\mathrm{H_2}}$ are partial pressures of $\mathrm{As_4}$, GaCl and $\mathrm{H_2}$ respectively, and T is the deposition temperature. The parameters, x_1-x_6, are estimated using nonlinear least-squares by minimizing the objective function defined as the square of the difference between model predictions, $F(x, x_m)$, and experimental data, y_m.

$$\min_x \|F(x, x_m) - y_m\|_2^2 \tag{3.38}$$

where x represents the estimated parameters, i.e., x_1-x_6. x_m is the measured value of the depositions temperature and the gas-phase partial pressures, and y_m is the measured growth rates for this case. **Table 3.2** lists the initial guesses, estimates and confidence intervals of the logarithmized parameters:

Table 3.2 Outputs of parameter estimation

Parameters	x_1	x_2	x_3	x_4	x_5	x_6
Initial values	-22.9445	4.8322	-19.3786	4.7359	-34.7285	4.9848
Estimates	-23.6271	4.8325	-20.0587	4.7362	-35.4133	4.9850
Confidence interval	11.3795	0.1936	9.6832	0.2091	11.9612	0.1425

The confidence intervals for the parameters are large, especially for x_1, x_3, and x_5. **Figure 3.2(a)** compares the model predictions and experimental data (Figure 3 in the reference paper[64]). Each of the curves gives the growth rates of GaAs as a function of reciprocal deposition temperature for growth operated near one atmosphere and with fixed As_4 composition. The composition of GaCl is varied for the different curves. As shown in the figure, the predicted and experimental data show similar trends: the growth rate increases with temperature at lower temperatures, reaches a maximum, and decreases at higher temperatures. The location of the maximum as predicted by the model differs somewhat from the measured data. Moreover, the reaction model does not show a maximum with increasing GaCl partial pressure, a behavior caused by the competitive adsorption of the gas species in the kinetically-limited growth regime.

Converted from **Equation 3.37** and parameters x_1-x_6, the nominal values of N_1, D_1 and D_2 in **Equation 3.33** can be obtained. These lumped terms turn out to be in the form of $\hat{A}(\frac{T}{T_{ref}})^b \exp(\hat{E}/T)$, where T is the growth temperature, T_{ref} is 1 [K], $\hat{A}$ is a lumped pre-exponential factor, $\hat{E}$ is an energy term scaled by gas constant, and b is temperature exponent. The values of $\hat{A}$, $\hat{E}$, and b for each of N_1, D_1 and D_2 are listed in **Table 3.3**.

Other parameters are estimated similarly from experimental epitaxial growth studies of GaInAs,[93,94] GaAsP,[90,95] and GaInP.[96]

Studies by Conrad et al.[93] and Jacobs et al.[94] provide measurements of $Ga_xIn_{1-x}As$ alloy composition as a function of GaCl gas-phase composition at two temperatures. The

objective function is minimized based on composition data rather than growth rate data. **Figure 3.2(b)** compares the predicted alloy compositions of $Ga_xIn_{1-x}As$, i.e., x, versus group III gas-phase composition to the measured values. The model predictions capture the concave functional dependence of the solid composition on the gas composition at the two different growth temperatures.

Studies by Belouet[95] and Ban et al.[90] provide both the alloy composition and growth rates of $GaAs_yP_{1-y}$ over a range of deposition temperatures at different flow rate ratios of AsH_3 to the sum of AsH_3 and PH_3. A similar parameter fitting procedure is performed. The composition and growth rate predicted from the model are compared with the corresponding measured data in **Figures 3.2(c)** and **3.2(d)**, respectively. From **Figure 3.2(c)** it is clear that the solid-phase composition is a strong function of the gas-phase composition but is a rather weak function of the deposition temperature. **Figure 3.2(d)** illustrates that the epitaxial growth rate of the GaAsP alloy also exhibits similar trends as the growth of GaAs (shown in **3.2a**). It is therefore reasonable to infer that the reactivities of GaCl with As and P precursors are roughly equivalent at least under these experimental conditions.

A study conducted by Sigai et al.[96] presents the $Ga_xIn_{1-x}P$ solid composition as a function of the group III gas-phase composition at two temperatures. **Figure 3.2(e)** compares the experimental results and the fitted model predictions. These results match satisfactorily. The model indicates that to reach a solid-phase composition of 0.5, a large flowrate ratio of InCl to GaCl is required. The $Ga_xIn_{1-x}P$ with the solid composition x equal to about 0.5 is an attractive III-V semiconductor material and has been widely used in III-

V devices because of its wider bandgap while lattice matched to GaAs. This model provides useful guidance in the selection of process operating conditions for the growth of the GaInP layer monolithically upon a GaAs layer with few lattice defects.

It should be noted that some of the model parameters cannot be estimated from the data available in the literature. We estimate approximate values for these parameters, D_3 and D_6, by setting them identical to D_2 and D_5, respectively. Finally, **Table 3.3** lists all of the kinetic parameters used subsequently in this work.

An accurate kinetic model is important for designing and optimizing HVPE reactors. Given the scarcity of the experimental data, however, a semi-empirical model for the growth rate has been established. But this model does capture the general characteristics of the HVPE growth of III-V compound semiconductors. As more accurate kinetic measurements are obtained, the kinetic model can easily be updated to obtain more accurate process designs.

(a)

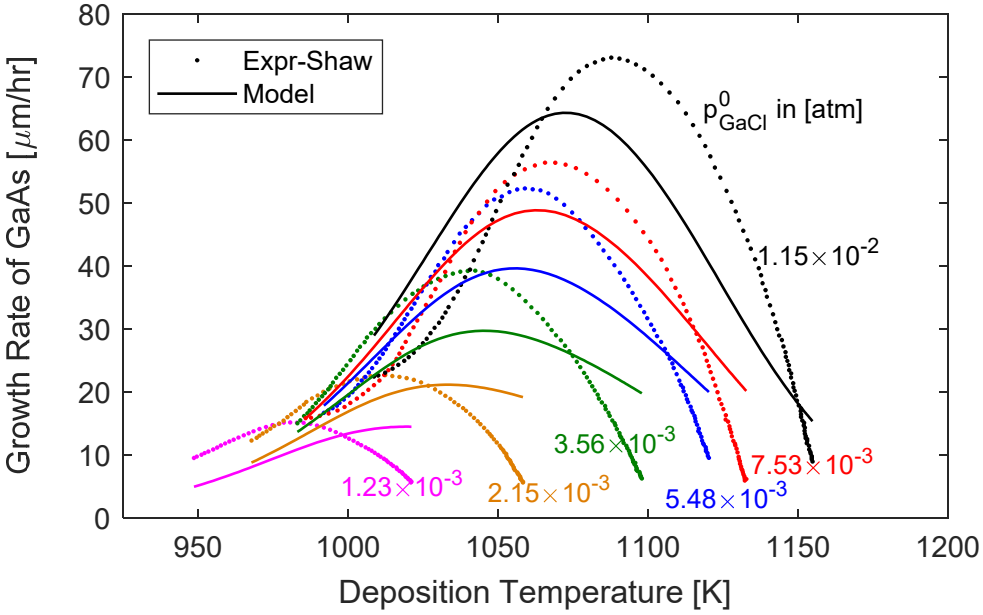

(b)

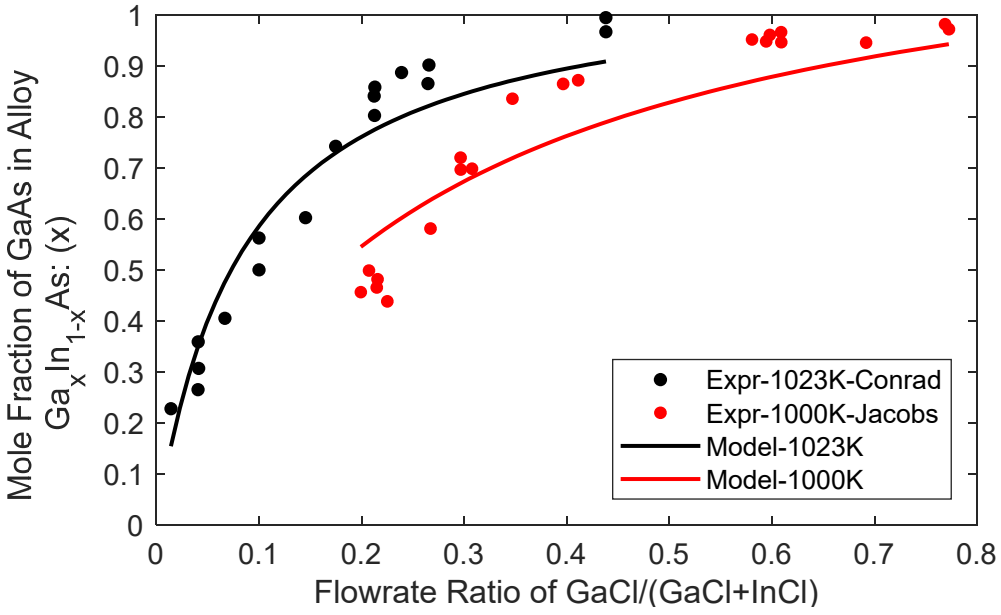

Figure 3.2 Comparison of growth results between derived rate law model and reported experimental data[64,90,93–96]

Figure 3.2 continued

(c)

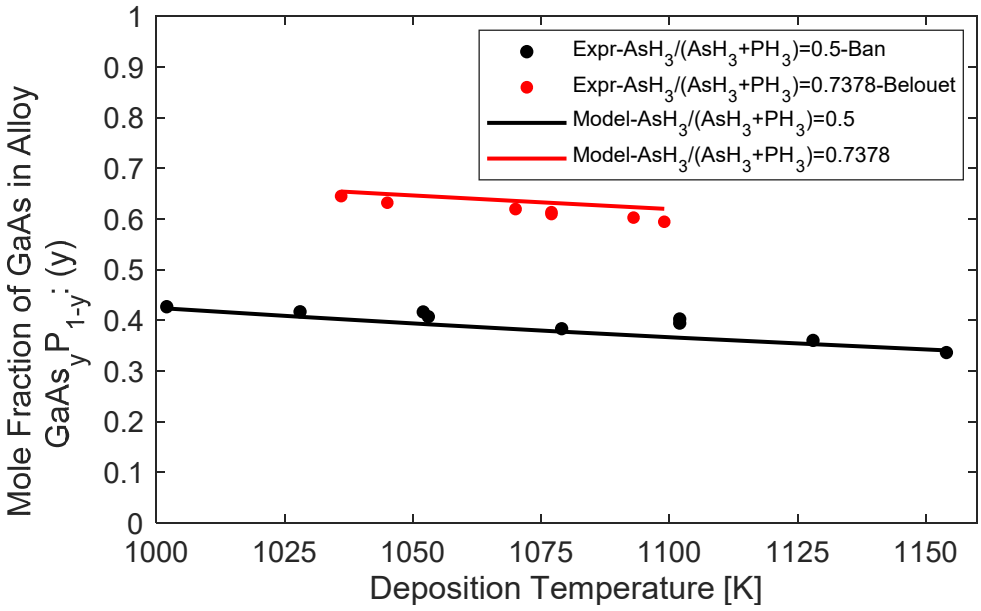

(d)

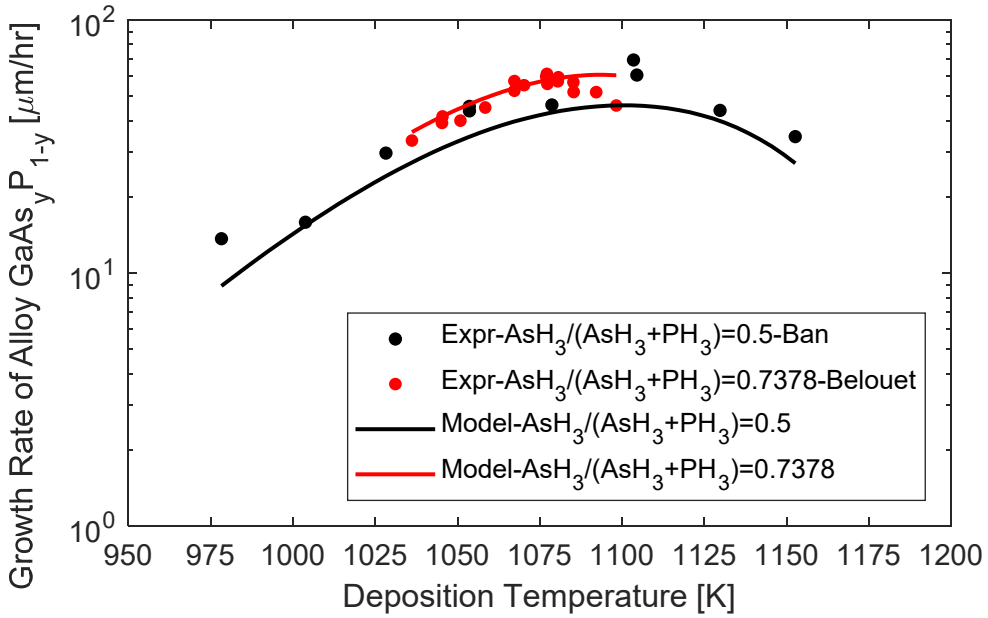

Figure 3.2 continued

(e)

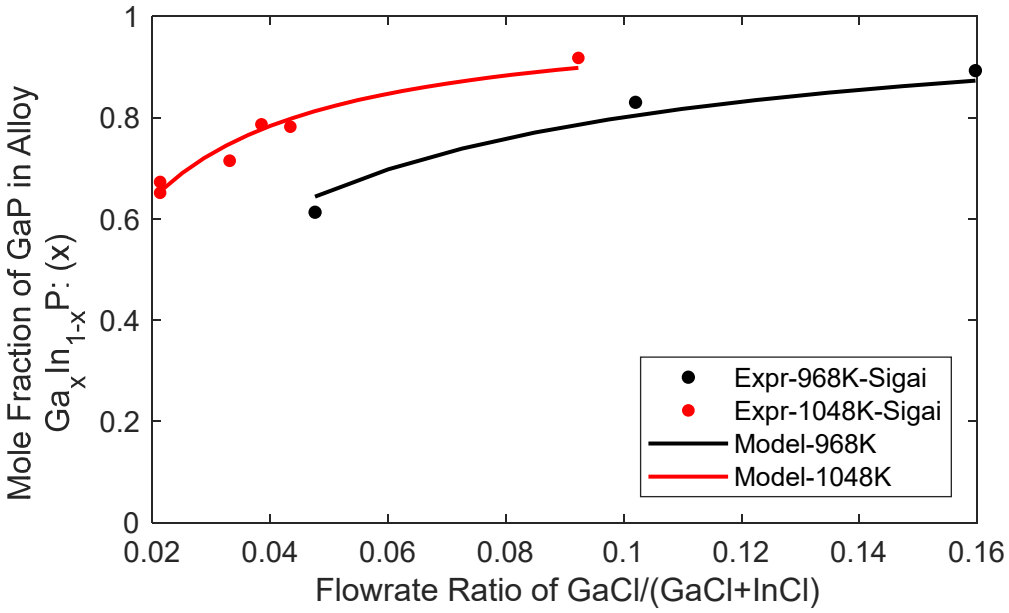

Table 3.3 Parameters for the kinetic model equations

Lumped parameter	Estimated expression $\hat{A}(\frac{T}{T_{ref}})^b \exp(\hat{E}/T)$		
	$\hat{A}$	b [1]	$\hat{E}$ [K]
N_1	5.39×10^{-36} [$\frac{m^7}{mol^2 \cdot s}$]	1.5	75546
N_2	1.86×10^{-55} [$\frac{m^7}{mol^2 \cdot s}$]	1.5	118791
N_3	1.06×10^{-34} [$\frac{m^7}{mol^2 \cdot s}$]	1.5	72874
N_4	3.03×10^{-41} [$\frac{m^7}{mol^2 \cdot s}$]	1.5	83992
D_1	2.57×10^{-21} [$\frac{m^3}{mol}$]	-0.5	62033
D_2	9.32×10^{-41} [$\frac{m^6}{mol^2}$]	0.5	104156
D_3	9.32×10^{-41} [$\frac{m^6}{mol^2}$]	0.5	104156
D_4	1.288×10^{-18} [$\frac{m^3}{mol}$]	-0.5	57667
D_5	1.055×10^{-30} [$\frac{m^6}{mol^2}$]	0.5	92356
D_6	1.055×10^{-30} [$\frac{m^6}{mol^2}$]	0.5	92356

3.5 Solution Method

The reactor model is implemented and solved numerically using the FEM-based commercial software, COMSOL Multiphysics®,[76] with an unstructured mesh. Grid sensitivity studies are performed for each case study to ensure the independence of the solution on the mesh scheme and size. It is time- and resource-consuming to solve the entire time-dependent, three-dimensional model; therefore, simplifications are useful. Especially at the earlier stage, models in two-dimensional geometry and/or at steady state are solved and analyzed to provide a quick qualitative understanding of the system's main characteristics.

Cases that involve the mesh moving, deforming and remeshing are the most computational-intensive. At each time step, the translation of the substrate leads to a change in the shape of the domain boundary and the corresponding mesh profile. Instead of solving the mesh deformation in the entire domain, we partition the modeling space into several subdivided domains to reduce the computational cost. As illustrated schematically in **Figure 3.3**, the entire domain can be divided into three subdomains, where different mesh deformation schemes are specified.

The white subdomain including the region around the substrate is finely meshed initially and the mesh is assigned a linear translating velocity that is defined by the speed of the moving belt. The mesh in the dark grey subdomains at both sides of the white region is allowed to deform when the white domain displaces from its original location, thereby simulating the scenario of a belt moving through the deposition assembly. The mesh is

fixed in the light grey subdomain that is located far from the moving belt and the substrate surface. A continuity boundary condition is applied at the interface between the top and bottom subdomains (separated by the dashed line in **Figure 3.3**) because the different mesh velocities cause the mesh discontinuity. We confirmed that the results are not affected by the assignment of the subdomains, especially the selection of the white subdomain. To alleviate the distortion of mesh elements, an automatic remeshing technique is used. The grey subdomain remeshes when the distortion reaches an upper limit rather than at each time step. The solution of the model is then resumed on the updated mesh.

(a)

(b)

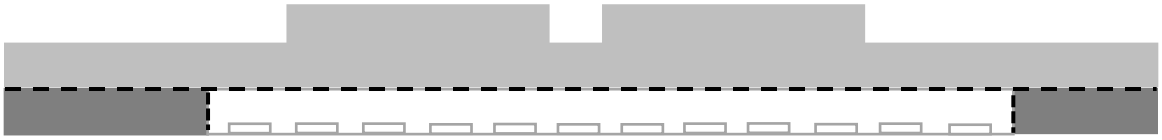

Figure 3.3 Schematic of the subdivision of the computational domain (a) and its evolution over time (b)

3.6 Film Properties

From the solution of the reactor model, properties of the film deposited on the substrate can be evaluated. The rate of change of film thickness θ is simply the growth rate of the film.

$$\mathcal{G} = \frac{d\theta}{dt} \tag{3.37}$$

It is the sum of the production rates of GaAs, GaP, InP and InAs scaled by their respective densities.

$$\mathcal{G} = \frac{R_{\mathrm{GaAs}}}{\rho_{\mathrm{GaAs}}} + \frac{R_{\mathrm{GaP}}}{\rho_{\mathrm{GaP}}} + \frac{R_{\mathrm{InP}}}{\rho_{\mathrm{InP}}} + \frac{R_{\mathrm{InAs}}}{\rho_{\mathrm{InAs}}} \tag{3.38}$$

The film thickness, θ, can be computed from **Equations 3.33-3.36**, **3.37**, **3.38**.

The instantaneous composition of the top-surface film is determined by the growth rate of each possible binary component relative to the overall growth rate.[97]

$$x_{\mathrm{GaAs}} = \frac{R_{\mathrm{GaAs}}}{R} \qquad x_{\mathrm{InAs}} = \frac{R_{\mathrm{InAs}}}{R} \qquad x_{\mathrm{GaP}} = \frac{R_{\mathrm{GaAs}}}{R} \qquad x_{\mathrm{InP}} = \frac{R_{\mathrm{InP}}}{R} \tag{3.39}$$

where R is total growth rate (or the growth rate of alloy).

$$R = R_{\mathrm{GaAs}} + R_{\mathrm{GaP}} + R_{\mathrm{InAs}} + R_{\mathrm{InP}} \tag{3.40}$$

Once the composition of each solid species is known, the alloy film can be succinctly denoted as $\mathrm{Ga_xIn_{1-x}As_yP_{1-y}}$. In this notation, x is the composition of Ga atom in group III atoms ($\mathrm{x} = x_{\mathrm{GaAs}} + x_{\mathrm{GaP}}$) and y is the composition of As atom in group V atoms in the film ($\mathrm{y} = x_{\mathrm{GaAs}} + x_{\mathrm{InAs}}$).

The non-uniformity of the growth rate leads to variations in the thickness and composition profiles in the films, which can be measured in multiple ways. Here we assess

the non-uniformity of the film thickness as $\frac{\theta_{\max}-\theta_{\min}}{\theta_{\max}}$,[98,99] where $\theta_{\max}$ and $\theta_{\min}$ denote the values of the maximum and the minimum thickness over the wafer, respectively.

Besides high spatial uniformity, a sharp composition interface between different layers is another critical product objective for developing a multi-zone continuous HVPE reactor system. Experimentally, interfacial composition transition in multilayer heterostructures may be characterized using transmission electron microscopy (TEM), high resolution x-ray diffraction (HRXRD), and atom probe tomography (APT).[100,101] In this work, this interfacial sharpness is evaluated by the distance in film over which the solid composition changes from the composition of one material to the composition of another material. For example, the interfacial transition distance in a GaAs/GaInP bilayer can be determined as the distance over which the Ga component changes from 100% to 50% (to within ±2%) and As from 100% to 0%. A smaller transition distance means a sharper interface.

3.7 Conclusions

In this chapter, the methodology to computational design of a continuous HVPE reactor is developed. Based on the general framework of CFD modeling of CVD reactors, this work updates the moving mesh feature to model the dynamics of substrate movement during continuous growth and presents a semi-empirical kinetic model for HVPE growth of GaAs semiconductor and related alloys to relate the growth rate with gas-phase conditions. Incorporating the kinetic model, the resultant reactor model establishes the

relationship between the film properties and the growth conditions which is strongly dependent on the reactor geometry, therefore can be served as a powerful tool aiding the reactor and process design. It is also noteworthy that this model is formulated based on a series of assumptions, therefore extending it to other growth conditions requires cautions. For example, when the precursors are concentrated with respect to the carrier gas, the mass transfer and fluid dynamics are fully coupled, and the properties of the mixture are dependent on the gas-phase composition. Under this circumstance, the diffusive transport of the gas-phase species may require Stefan–Maxwell formulation or a less rigorous but computationally favorable mixture-averaged formulation. If the reactor geometry is engineered to induce turbulence, the flow field needs to be described by one appropriate turbulence model, such as k-ε model or k-ω model, depending on the flow characteristics and computational resource.

3.8 Appendix

Notation

Subscript

i: gas-phase species

s: surface

c: carrier gas

b: belt

in: inflow or inlet

l: leaking

x, y, z: direction in Cartesian coordinate system

x, y in $Ga_xIn_{1-x}As_yP_{1-y}$: Ga, As atom composition

Variables

ρ: Density of gas mixture

D: Diffusion coefficient

$\mathbf{v}$: Material velocity

R: Production rate

$\hat{\mathbf{v}}$: Mesh velocity

p: Pressure

$\mathbf{v_c}$: Convective velocity

p_0: Reference pressure

M: Molar mass

θ: Film thickness

μ: Viscosity

$\mathcal{G}$: Growth rate of a film

T: Temperature

$\hat{A}$: Lumped pre-exponential factor

c: Concentration

T_{ref}: Reference temperature,1 [K]

$\mathbf{I}$: Identity matrix

b: Temperature exponent

$\hat{E}$: Lumped energy term scaled by gas constant

$\mathbf{n}$: Outward pointing unit vector normal to the boundary

4. HVPE GROWTH OF III-V MULTILAYER HETEROSTRUCTURE

4.1 Introduction

To model the growth system involving HVPE deposition of various III-V semiconductors, we have developed a semi-empirical kinetic model and validate it based on a variety of experimental data sources. This reaction model is coupled with three-dimensional transport model as boundary conditions on the substrate surfaces to constitute a complete reactor model, which relates process outputs (including film thickness, uniformity, composition, etc.) with process inputs (including reactor geometry, operating conditions, etc.).

Equipped with the modeling tool, in this chapter, we investigate the influences of the substrate movement and the separation zones on the process characteristics and the corresponding product properties. The operation and capability of the continuous HVPE reactor is further demonstrated through fulfilling the task of growing III-V multilayer heterostructures for a specific solar device.

4.2 Effect of Substrate Movement

To study the effect of the substrate movement on the transport of gas-phase species and the film growth, one time-dependent simulation that models the continuous HVPE growth of a GaAs-GaInP bilayer structure is carried out.

In the calculations, a reactant gas mixture for depositing GaAs is flowed into the first deposition chamber (see **Figure 2.3**) at a flow rate of 0.35 m/s and another reactant gas mixture for depositing GaInP is flowed into the second deposition chamber at a flow rate of 0.35 m/s. The flowrate of purge gas (pure H_2 in this study) through the top inlet of the separation zone is 0.2 m/s. The speed of the moving belt is 0.02 m/s. The height and the length of the deposition zones are selected as 0.125 m and 2 m respectively. The height and the length of the separation zone are 0.0625 m and 0.5 m respectively. The model is solved over a time length of 75 s.

Figure 4.1 shows the change of the gas-phase GaCl concentration with time at several spatial locations in the deposition zones while epitaxial growth is taking place on the substrates, which are carried by a belt translating in the longitudinal direction. Comparing subplot **(c)** to the subplot of **(a)** or **(b)**, it is shown that the amplitude of the sine curve is smaller (smaller range of variation) and the magnitude of the average concentration is greater for the spatial location that is farther from the surface of the substrates. The GaCl concentration of each curve exhibits nearly exact periodicity over the time range. Each of these curves has almost identical period (denoted as $\mathcal{T}$), 25 second, that is equal to the time length required for one wafer moving from its original spatial location to the location that initially belongs to the preceding wafer, which is predetermined by the speed of the moving belt. The growth on the substrates causes the local depletion of the gas-phase species, and the movement of the substrates of circular shape causes the periodic fluctuations of concentration profile in the reactor.

The quality of the final product is the important characteristic for the evaluation of the process but tracking one wafer from entering the growth system to leaving as final product in a continuous HVPE system is computationally expensive and unnecessary as a proof-of-concept. The periodicity of the gas-phase variations justifies that when the continuous growth is under steady operation, one period of the full time-dependent solution is adequate to represent the solution over the entire time horizon. Therefore, the movement of n substrates aligned in the deposition zones can be solved for a time range spanning only one $\mathcal{T}$, and the solutions of these different substrates are post-processed to represent that of one single wafer in the entire time range spanning $n\mathcal{T}$.

(a)

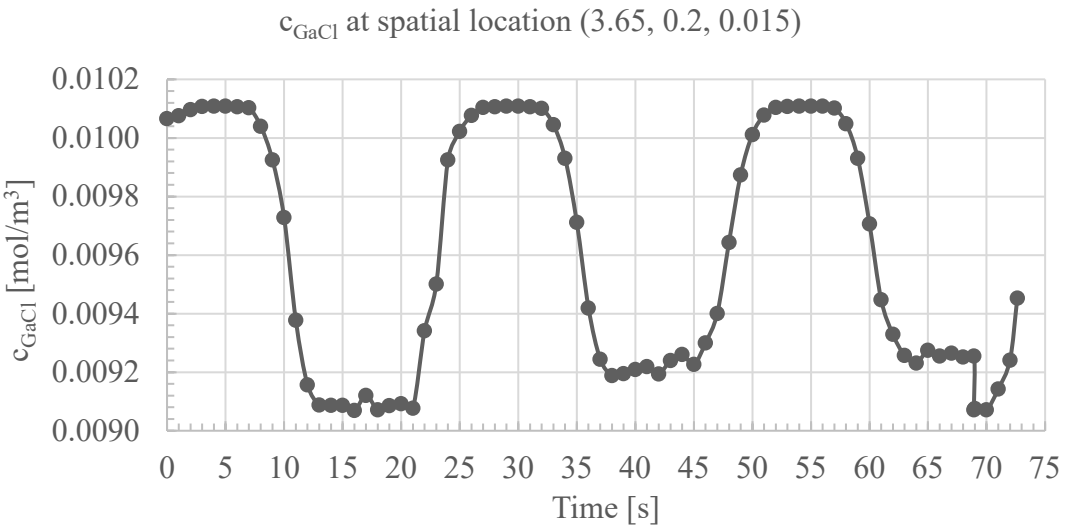

(b)

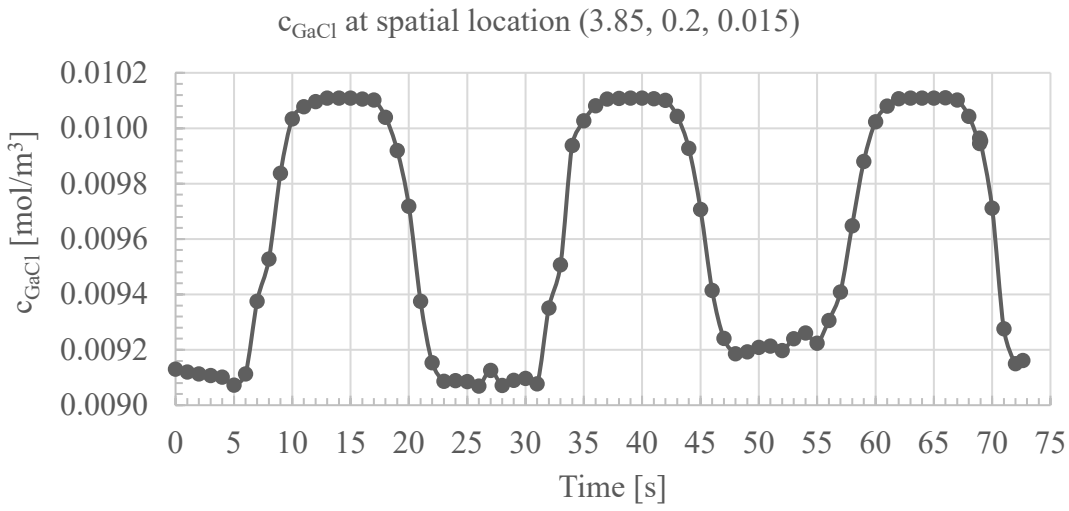

Figure 4.1 Concentration of GaCl at several spatial locations during continuous growth on moving substrates: (a-c) spatial locations in a deposition zone for GaAs, (d) spatial location in a subsequent deposition zone for GaInP, the coordinates of these locations are given in the title of each subplot

Figure 4.1 continued

(c)

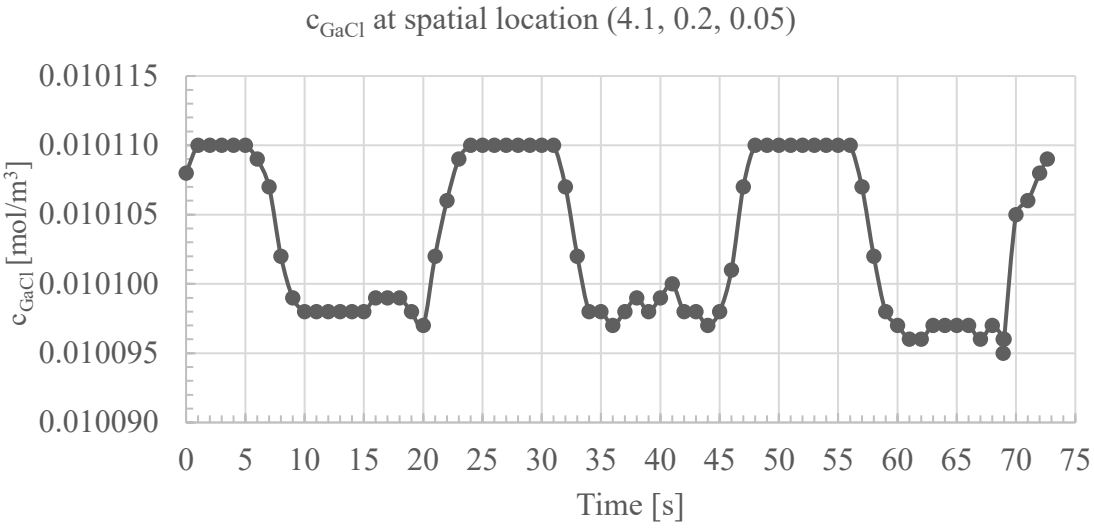

(d)

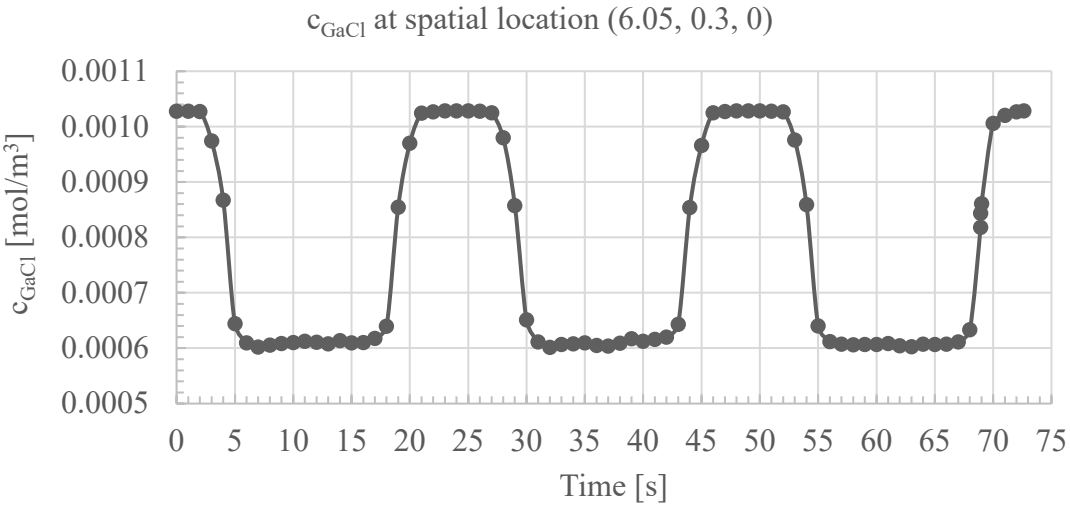

Figure 4.2 shows the profiles of the total growth rates as well as the substrate movement at several time steps during a continuous growth of a heterostructure.

The deposition zone 1 is specified to grow GaAs and deposition zone 2 is for GaInP. Whenever the substrates move into the separation zone, the growth rates decrease to zero. Subplots **(b)** and **(d)** show the transient profile when some substrates are partially located in both the deposition and separation zones. The transitions aligning with the geometric boundaries of the different zones demonstrate an effective separation. It can be observed that subplots **(a)** and **(c)** present nearly identical results, which further confirms the periodic dynamics of the growth system discussed before.

(a)

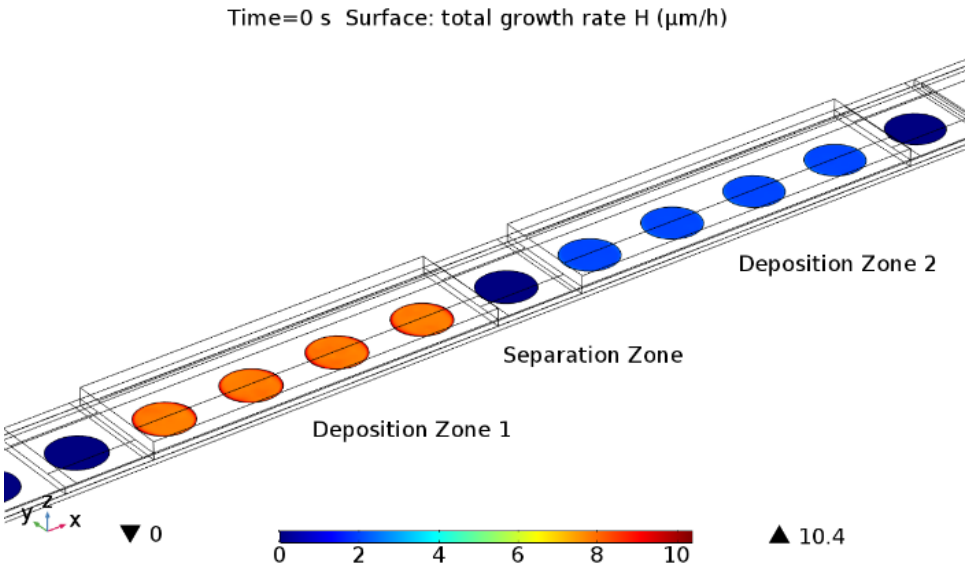

(b)

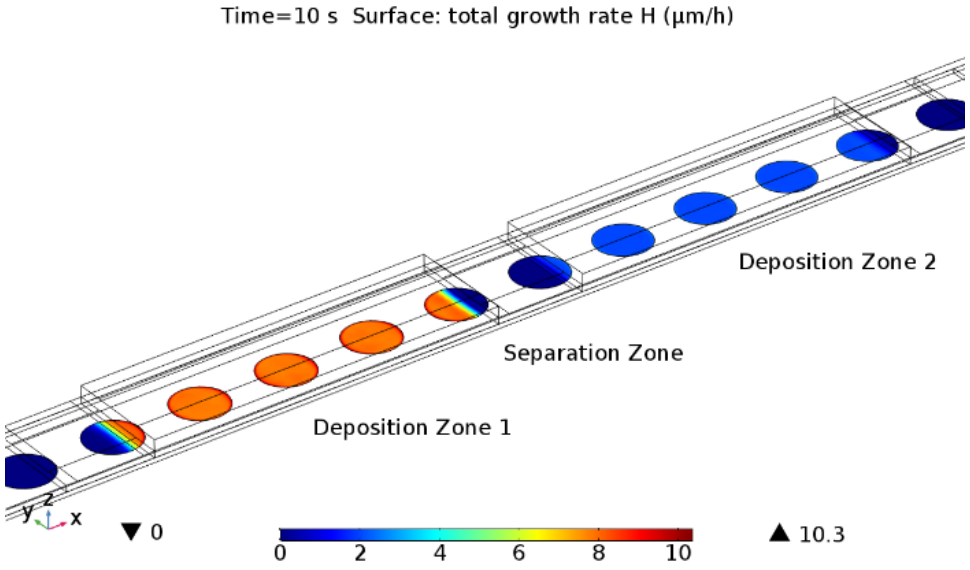

Figure 4.2 Profile of total growth rate during continuous operation

Figure 4.2 continued

(c)

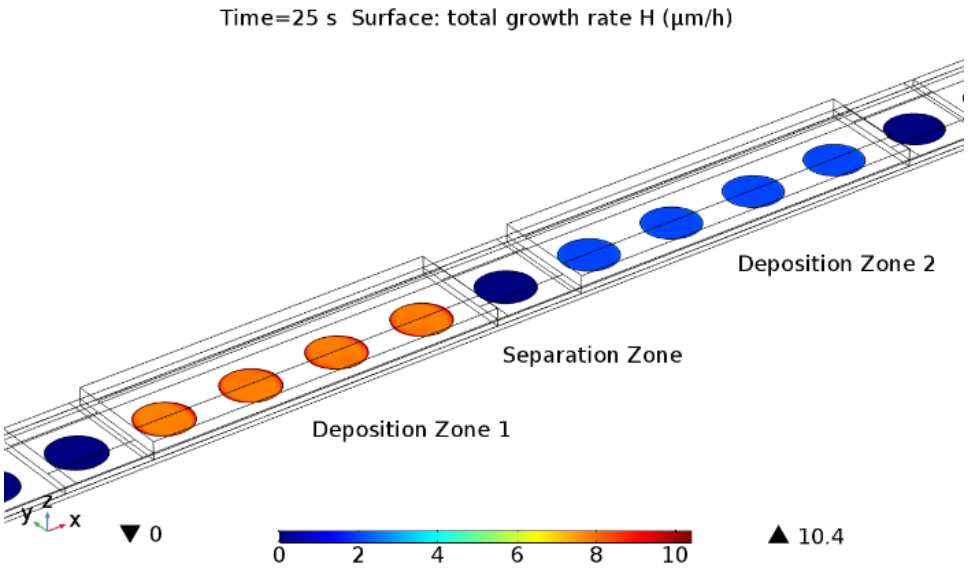

(d)

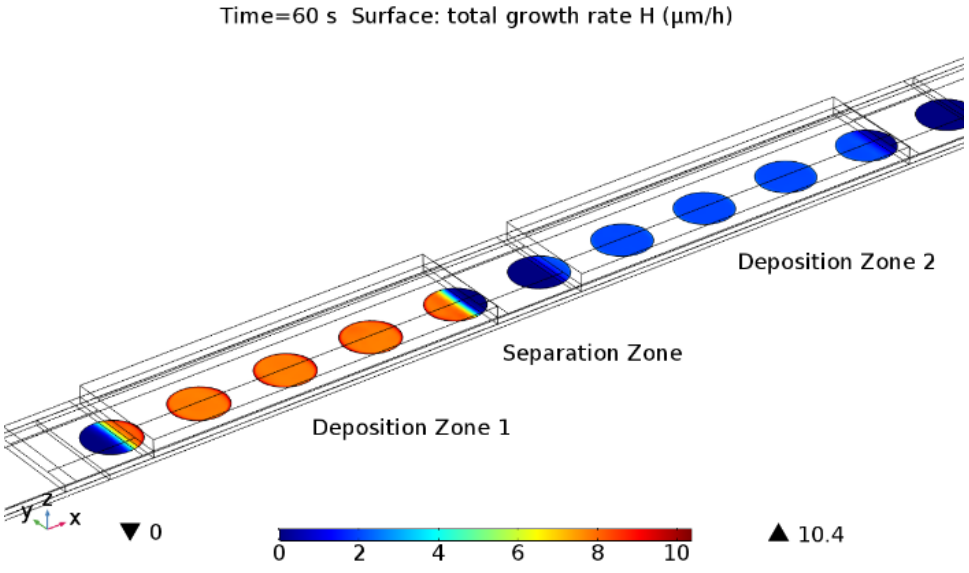

4.3 Separation Zone and Interface Abruptness

Interfacial abruptness is critical to the quality of the device. Forming a sharp interface is a technical challenge for high-throughput HVPE systems. In the present configuration, a separation zone is placed between different deposition zones to quench the growth without interrupting the continuous operation. Both the operating condition and the geometry of the separation zone affect the efficacy of separation, and therefore the interfacial quality.

This study is carried out through the simulation of growing a GaAs-GaInP bilayer in a growth system with at least two deposition zones and one separation zone. In the calculations, a reactant gas mixture for depositing GaAs is flowed into the left deposition zone at a flow rate of 0.35 m/s and another reactant gas mixture for depositing GaInP is flowed into the right deposition zone at a flow rate of 0.35 m/s. The speed of the moving belt is 0.02 m/s. The height and the length of the deposition zones are selected as 1 inch and 2 m respectively. The length of the separation zone is 0.125 m. The height of the separation zone is varied from 0.1 inch to 1 inch for the case where there is no H_2 flowing in the separation zone. Then the height of the separation zone is fixed at 1 inch, and the effect of gas curtain and its flowrate is evaluated.

4.3.1 Height of separation zone

Figure 4.3 shows the profile of III-Cl species concentration near the separation zone when the separation zone is designed as a constricted region without H_2 flow. The subplots on the left column (**a**, **c**, **e**) show the profile of GaCl concentration while the

subplots on the right columns (**b**, **d**, **f**) show the profile of InCl concentration. From the top rows to the bottom, the height of the separation zone, h_{sep}, is decreasing. The plots illustrate the effectiveness of the separation is improved as the height of the separation zone is decreased.

Figure 4.4 further presents the composition variation (y-axis: Ga composition in subplot **a** and As composition in subplot **b**) across a 20-nm slice of bilayer GaAs-GaInP heterointerface (x-axis: height of deposited films) grown from the system without the operation of gas curtain at the separation zone. The height of the separation zone, h_{sep}, is varied between the different curves. The profile of each curve describes the interfacial transition region between two distinct material layers (GaAs in the lower layer and $Ga_{0.51}In_{0.49}P$ in the upper layer).

In subplot **(a)**, the transition region has been labeled for one of the curves (h_{sep} = 0.10 inch). The width of this region, δ, is defined as the distance between the point at which Ga composition starts to decay (from x = 1 in GaAs) and the point at which Ga composition stabilizes to the desirable value (x ≈ 0.51). Similarly, the width of the interfacial transition region can be determined for other curves as well as that for As compositions. Decreasing the height of the separation zone, the transition region becomes narrower. For the case of h_{sep} = 0.1 inch, a value of about 2 nm for Ga composition is achieved while the As composition shows a sharp step-function profile.

It should also be noticed that the curves deviate from each other in the x-axis. Curves with higher h_{sep} values shift in the direction of higher film height (positive x-axis

direction). Because a separation zone with a large h_{sep} cannot effectively block the convective transport of reactive species, it allows deposition to continue even when the substrates are in the separation zones. Due to the extra deposited material, the thickness of layers may exceed the product specification, which must be avoided in a well-controlled manufacturing process.

Lowering the height of separation zone can achieve a more abrupt junction with small transition region and effectively minimize undesired growth. This observation justifies optimizing the geometry of the separation zone to reduce process cost and achieve the desired degree of separation efficacy by decreasing the flow rate or not using a purge gas.

h_{sep} = 0.75 [inch]

(a) c_{GaCl} [mol/m^3] (b) c_{InCl} [mol/m^3]

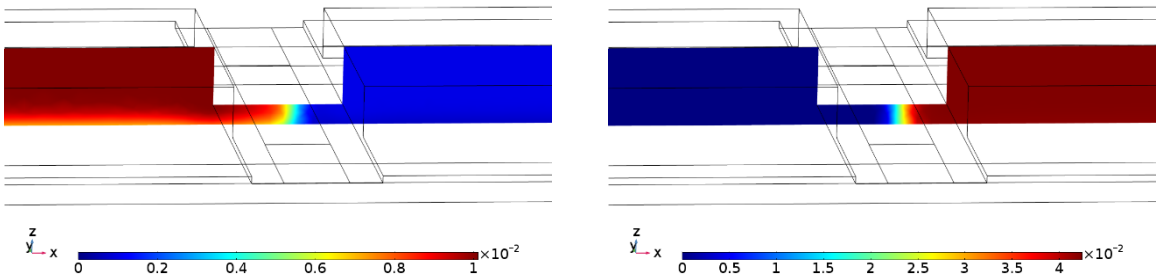

h_{sep} = 0.50 [inch]

(c) c_{GaCl} [mol/m^3] (d) c_{InCl} [mol/m^3]

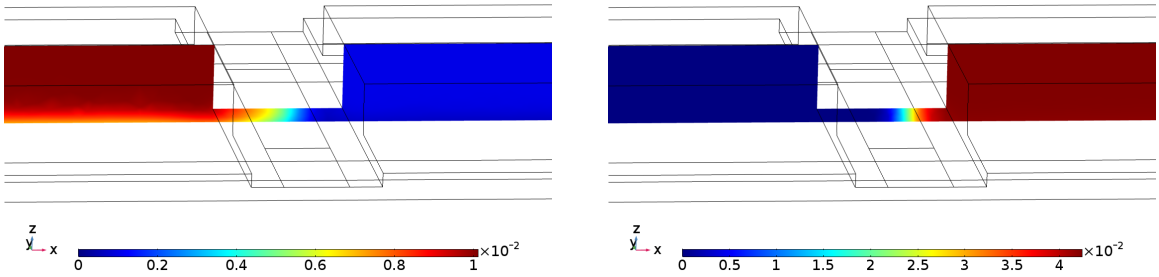

h_{sep} = 0.25 [inch]

(e) c_{GaCl} [mol/m^3] (f) c_{InCl} [mol/m^3]

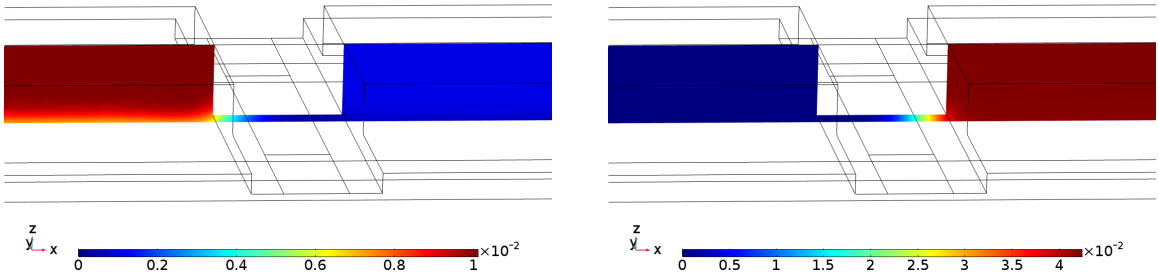

Figure 4.3 Profile of IIICl gas-phase composition near the separation zone

(a)

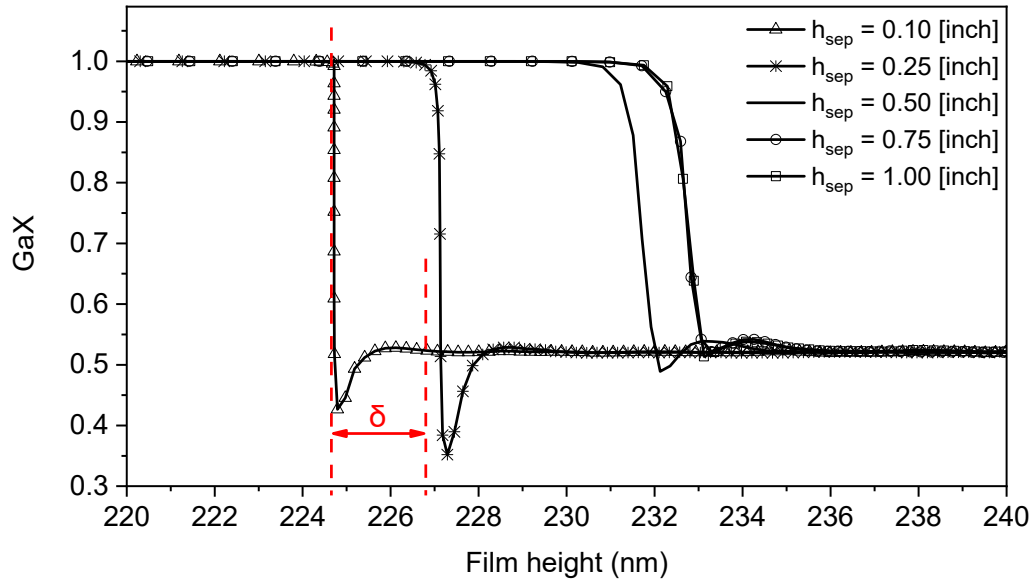

(b)

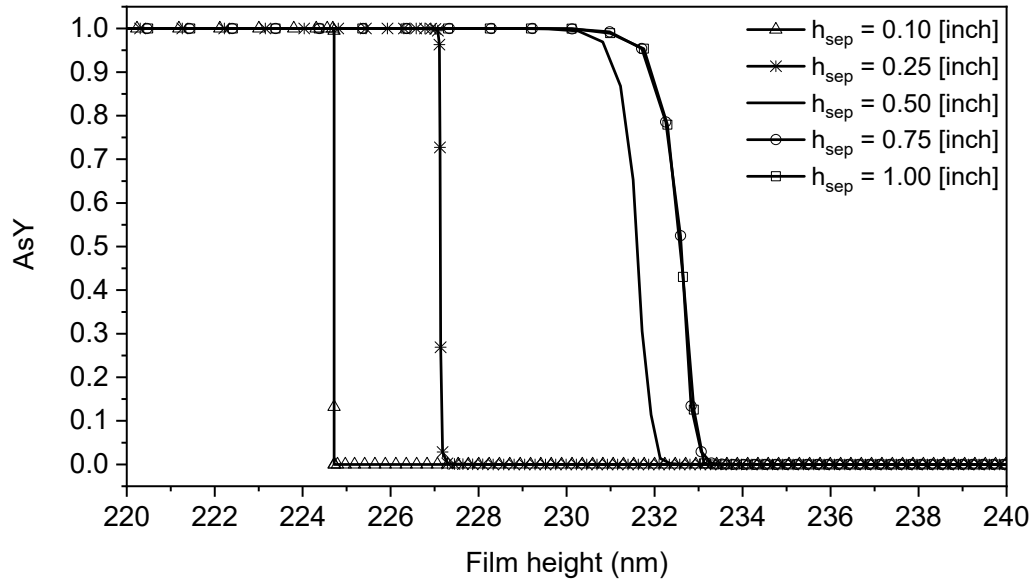

Figure 4.4 Composition variation in the interface region for cases without gas in separation zone: (a) Ga composition in solid, (b) As composition in solid

4.3.2 Gas curtain

Figure 4.5 shows analogous results from cases when the purge gas (pure H_2 in this study) is flowing through the separation zone at rates of 0.1 m/s and 0.2 m/s and the height of the zone is fixed at 1 inch. The rightmost curve in **Figure 4.5** shows the worst-case scenario for comparison. It is easily seen that applying the gas "curtain" improves greatly the heterointerface abruptness. Although applying gases is always an option, the flow rate should be tuned carefully given the geometry of the separation zone as well as the flowrate of gas in the adjacent zone, to avoid interfering with the growth in the deposition zones and wasting the purge gases.

(a)

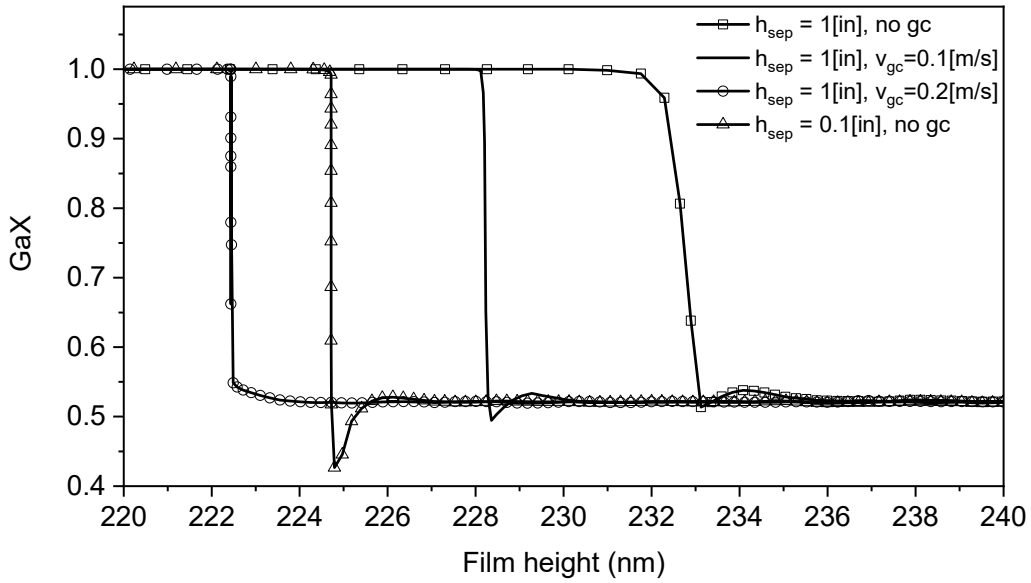

(b)

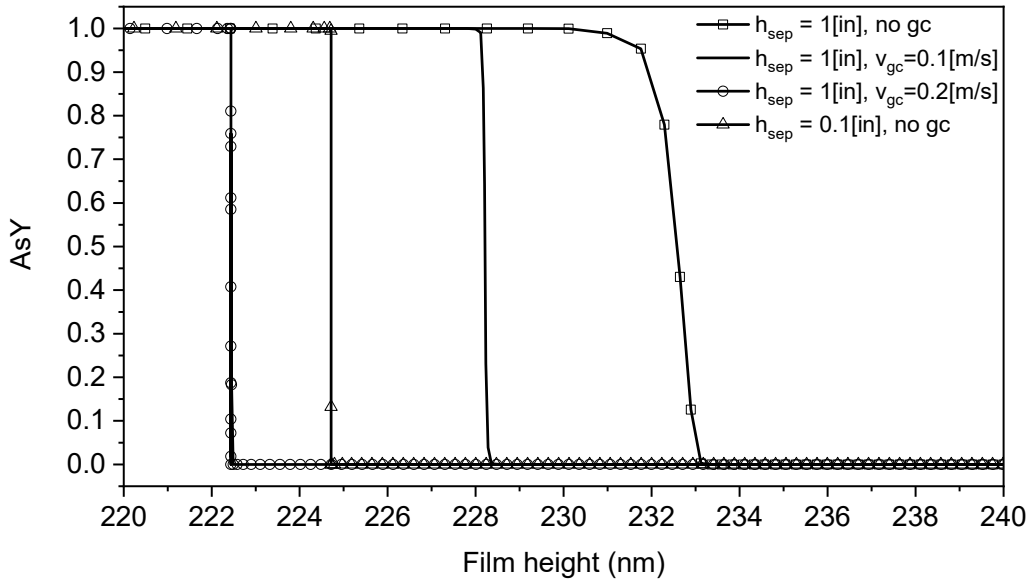

Figure 4.5 Composition variation in the interface region for cases with vs. without gas in separation zone: (a) Ga composition in solid, (b) As composition in solid

4.4 Growth of Multilayer Heterostructure

4.4.1 Analysis of operation mode and growth condition

The modeling tool is then applied to simulate the growth of a multilayer heterostructure in the continuous HVPE growth system.

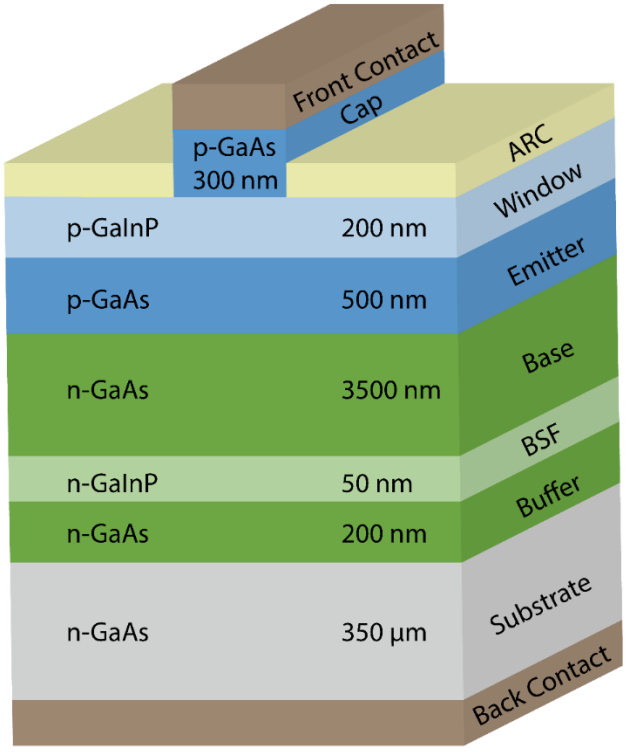

Figure 4.6 Structure of an example single-junction GaAs solar device (not drawn to scale)

As shown in **Figure 4.6**, the target device is a single-junction p-on-n GaAs-based solar cell constituted by n-/p-doped GaAs and lattice-matched GaInP epilayers.[102] The

composition and thickness of each layer are included in the figure. The p-GaInP and *n*-GaInP epilayers are used as the wide bandgap window layer and BSF layer, respectively. To fabricate this device, a piece of n-GaAs single crystal substrate is preprocessed and transferred into epitaxial growth system, in which six layers starting from n-GaAs buffer layer to the p-GaAs cap layer are successively deposited.

For growth in the continuous reactor, it is important to grow each epilayer with minimal discrepancies between the product and the specifications (shown in **Figure 4.6**) at high throughput. The uniformity of thickness over the wafer and the abruptness of composition change between two sequential layers are also crucial. The constraints imposed on the design of the growth system include the material specifications (i.e., the composition and thickness of each layer) and reactor model equations adapted to this specific geometry.

To well define this problem, we assume the substrates used in this study are round single crystal GaAs wafers with a diameter of 12 inches, and the speed of the moving belt in each zone and the spacing between two adjacent wafers are fixed and identical.

For this continuous reactor, throughput can be estimated as:

$$P = \frac{N}{L/U_{belt}}$$

where P denotes the throughput, N denotes the number of wafers in the growth reactor, L denotes the length of the growth reactor, and U_{belt} denotes the speed of moving belt.

The total number of wafers in the growth system can be approximated as:

$$N = \frac{L}{d_{sub} + x_{spac}}$$

where d_{sub} is the diameter of the substrate, and x_{spac} represents the spacing between adjacent substrates.

Therefore,

$$P = \frac{U_{belt}}{d_{sub} + x_{spac}}$$

Increasing the speed of the moving belt and decreasing the spacing between adjacent substrates can increase process throughput. However, operating the belt at high velocity may interfere gas flow pattern and deteriorate epilayer quality. Since in this study we mainly focus on the simulation rather than the optimization, baseline values are prescribed to the belt speed and the substrate spacing. These values are selected conservatively to ensure the elimination of impact from the belt and neighboring substrates, therefore the throughput may not reach its optimum. Nevertheless, the throughput of this setting is still better than that of the corresponding batch process.

Ideally for each deposition zone, we have the following relationship:

$$\frac{L_{dep}}{U_{belt}} = \frac{\theta}{H}$$

where L_{dep} is the length of the deposition zone, θ is the thickness of the epilayer grown in the specific deposition zone, H is the growth rate.

Once the geometry of the reactor, the operating condition of the moving belt, and the product specification are given, the growth rate in each zone is determined accordingly.

This relation also imposes constraint on the geometry of the reactor since the growth rate achievable in each zone must be in a reasonable range, typically 0.1-1 μm/min. **Table 4.1** lists the target growth rates given the length of each zone and the speed of the moving belt. **Figure 4.7** sketches the corresponding configuration of continuous HVPE reactor for the sequential deposition of six layers. The details about the geometries of deposition and separation zones as well as the operation of this process have been elaborated in **Chapter 2**, therefore are omitted here for brevity. The third deposition zone shown in **Figure 4.7** includes four units of deposition chamber. This is because the base layer is thicker than any other layers and a modular configuration is preferred over designing deposition zones with different lengths. The length of one standard deposition chamber is selected as 2 m in this study. If counted starting from steady operation, daily production of 12-inch wafer with the target heterostructure through this growth system is approximately 3456 pieces (i.e., 2.5 pieces of wafer per minute, conservative estimation).

Table 4.1 Analysis of operation mode

Deposition zone No.	Layer	Material	Deposition zone length L_{dep} [m]	Product thickness θ [μm]	Belt speed U_{belt} [m/s]	Growth rate H [μm/h]
6	Cap	GaAs	2	0.3	0.02	10.8
5	Window	GaInP	2	0.2	0.02	7.2
4	Emitter	GaAs	2	0.5	0.02	18
3	Base	GaAs	8	3.5	0.02	31.5
2	BSF	GaInP	2	0.05	0.02	1.8
1	Buffer	GaAs	2	0.2	0.02	7.2

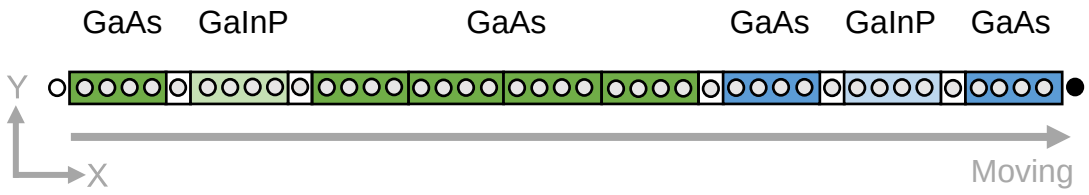

Figure 4.7 Schematic of continuous HVPE growth for target device

To achieve the designated growth rates, the growth condition in each deposition zone is adjusted using the reactor model. Instead of varying temperatures among different zones, it is preferable to adjust the flowrates of precursors to avoid thermal shock to the wafers. **Table 4.2** lists one set of growth conditions. It is noteworthy that in deposition zones for the growth of GaInP, InCl:GaCl ratio (the ratio of InCl gas concentration to GaCl gas concentration) needs to be well adjusted to achieve the desired alloy composition.

Table 4.2 Growth condition used in this case study

Deposition zone No.	Goal			Condition		
	H_{GaAs} [μm/h]	H_{GaP} [μm/h]	H_{InP} [μm/h]	T_{dep} [K]	x_{GaCl} [%]	x_{InCl} [%]
6	10.8			1023.15	0.1337	
5		3.206	3.994	1023.15	0.0356	1.4851
4	18			1023.15	0.2574	
3	31.5			1023.15	0.7426	
2		0.801	0.999	1023.15	0.0087	0.3574
1	7.2			1023.15	0.0851	

The entire model with the simplification mentioned in previous sections are then applied. Instead of modeling one wafer through the whole system (≈18 min), we model

the growth within the time range for one wafer moving from its original location to the next (25 s).

4.4.2 Growth rate and film properties

The growth results in each deposition zone are listed in **Table 4.3**. The growth rates vary around the goal values, as well as the composition of GaInP layers. The non-unformity of growth rates is caused by the edge effect of gas-phase mass transfer and leads to the non-uniformity of film thickness. This will be further mentioned soon.

Table 4.3 Comparison of simulated growth results and the goal

Deposition zone No.	Goal			Result			
	H_{GaAs} [μm/h]	H_{GaP} [μm/h]	H_{InP} [μm/h]	H_{GaAs} [μm/h]	H_{GaP} [μm/h]	H_{InP} [μm/h]	Ga composition
6	10.8			10.4-10.8			
5		3.206	3.994		3.08-3.32	3.97-4.01	0.491-0.508
4	18			17.5-18.2			
3	31.5			31.5-32.1			
2		0.801	0.999		0.768-0.831	0.999-1.02	0.489-0.505
1	7.2			7.01-7.46			

Table 4.4 shows the thickness of the grown film (measured at the center point) over the substrate at the end of each deposition zone. The results from the simulated growth basically meet the material specifications. With the aid of the model, the growth conditions could be finely tuned to minimize the discrepancies between the simulated product and the specifications in the future work.

Table 4.4 Thickness of deposited film at the end of each deposition zone

Time step [s]	Equivalent to the *i*th deposition zone product	Goal thickness [nm]	Result (Approx.) [nm]
125	1	200	190
250	2	250	245
675	3	3750	3895
800	4	4250	4420
925	5	4450	4620
1050	6	4750	4995

Thickness of deposits at every spatial location on one substrate can be obtained by integrating the growth rate (in height/time) over a time range of interest. To thoroughly evaluate the process performance, wafer-to-wafer and within-wafer uniformities of thickness and composition can be assessed. **Figure 4.8** shows the thickness and its uniformity of a final product grown in the continuous system. The thickness of the film

increases at the edge of the substrate. This edge effect is expected.[78] The non-reacting surface of the moving belt causes a large species concentration gradient locally near the edge, leading to the lateral diffusion of reactants into the growing surface and the extra deposition. This effect generally cannot be avoided in the growth system since there is always a concentration difference between the substrate and the belt. But designs that reduce this effect are possible. In the semiconductor industry, edge exclusion (removal) around the wafer is employed to obtain a final product with high uniformity. For example, as shown in **Figure 4.8(b)**, the non-uniformity is decreased by half if a 1 cm outer annulus is removed. In the future work, the operating conditions and geometry of the deposition zones will be systematically optimized to further improve the uniformity.

(a)

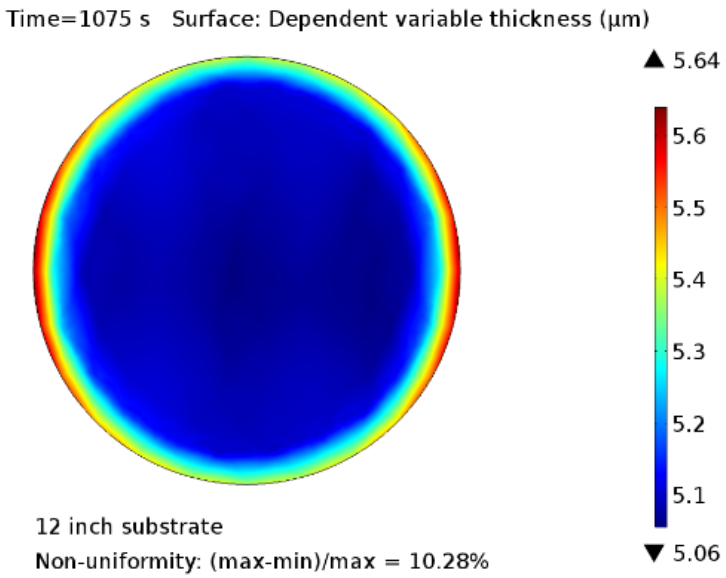

(b)

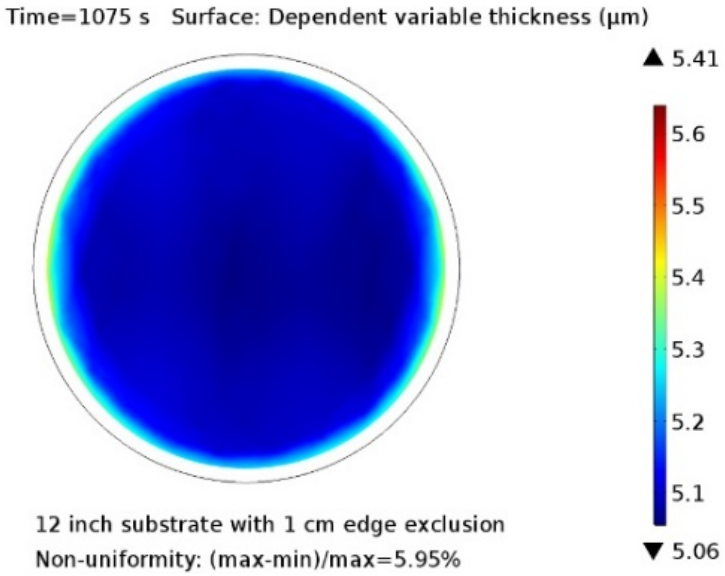

Figure 4.8 Thickness uniformity of the final film grown on a 12-inch substrate (a) without and (b) with edge exclusion

4.5 Conclusions

In this chapter, the model formulated in the **Chapter 3** is adopted to investigate the transport phenomena and the epilayer deposition in the growth system.

The effect of the substrate movement on the transport phenomena in the reactor is studied through a time-dependent simulation of the HVPE growth of a GaInP-GaAs bilayer solved over a relatively long duration of time. The variations of gas-phase concentrations at several representative sampled locations in the reactor exhibit periodic characteristics while the deposition is occurring on moving substrates. This periodicity can be used to simplify the solution of the model.

The modeling tool is applied to investigate the effect of the design variables of the separation zone on the abruptness of the interfacial composition transition in heterostructures. It is shown that a sharp interface can be produced by decreasing the height of the separation zone even without a gas curtain.

Lastly, the model is used to simulate the continuous HVPE growth of a multilayer structure in solar cells. The feasibility of continuous growth in the proposed system is verified.

Complemented with experimental design, the proposed model is a powerful tool to guide an efficient design of a new system or to optimize a current operation. Furthermore, the methodology of problem formulation and numerical techniques used in this work may also be extended to design and optimize a wide range of chemical vapor deposition systems.

5. SIMULATION AND ANALYSIS OF III-V HETEROSTRUCTURE SOLAR CELLS

5.1 Introduction

In order to address the technical challenge limiting the mass production of low-cost III-V photovoltaics by HVPE, we have proposed a high-throughput multi-zone growth system which controls the heterointerface formation using automatic growth interruption realized by separation zones. We have also developed a transport-reaction model to relate the multilayer film properties such as the uniformity of layer thickness and the abruptness of interfacial composition change with the operating conditions and reactor geometry. However, since the major application of this process is the production of III-V solar cells, it is essential to measure the performance of the process in term of device efficiency and to optimize the process for the growth of high-efficiency solar cell structures.

Therefore, in this chapter, we explore the approach of device modeling for the quantification of heterostructure quality in term of solar cell efficiency for the development of continuous HVPE process. We carry out the detailed numerical simulation of GaAs-based solar cells that can be grown through the proposed continuous HVPE to relate the device performance with the film structure and material properties. A prototype solar cell structure from the literature[50] is selected as the reference. This solar cell integrates a p^+-GaInP window layer and an n^+-GaInP back surface field layer to improve the collection efficiency of photogenerated carriers. Parametric studies based on this reference structure

are conducted to seek opportunities for solar cell optimization. The impact of interfacial abruptness in composition change at the interface of the GaInP window and GaAs emitter layers on the solar cell efficiency is investigated in detail. The result of this study can be used to quantify the performance of the continuous HVPE process in the interface control for the heterostructure growth. The continuous HVPE process can be further optimized using the reactor model in conjunction with the device simulation method developed in this work.

5.2 Method

The major tool adopted in this work is the device simulation program Atlas from the Silvaco TCAD suite.[103] This device simulator further includes multiple modules covering different physics and material systems. We mainly rely on the Blaze module for compound semiconductor device modeling and the Luminous module for the calculation of light propagation and absorption. The simulator numerically solves the Poisson and continuity equations in the computational domains of the solar cells that are subject to specific boundary conditions. The solution not only predicts the external characteristics such as the illuminated and dark J-V, the quantum efficiency and the reflectivity but also evaluates the internal quantities such as the carrier concentration, the recombination and generation rate, and the electron and hole currents.

In the present work, the major evaluation criterion is the conversion efficiency extracted from the J-V curve obtained under one-sun AM1.5G illumination (300K test temperature).

In the simulation, important physical models such as Fermi–Dirac statistics ("fermi", "ni.fermi"), Shockley–Read–Hall (SRH) recombination ("srh"), concentration-dependent mobility ("conmob"), Auger recombination ("auger"), radiative recombination ("optr"), bandgap narrowing effect ("bgn") and surface recombination are activated for the specific regions and materials.

The ray tracing method is adopted to model the light propagation and absorption in the multilayer heterostructure. Given the complex refractive index of the film material ($n-i\kappa$), this method uses the real part (n) to calculate the optical intensity at grid points and the imaginary part (κ) to compute the photogeneration rate.

In most simulations carried out in the present study, the following assumptions have been made to confine the number of uncertain variables:

(1) The front and back contacts are assumed to be ohmic in all cases;

(2) The influences of series resistance and shunt resistance, shading, photon recycling,[104,105] and free carrier absorption are not considered;

(3) The front and back reflections are considered only for the simulation of spectral response of the reference solar cell; while for other simulations the reflections at the front of the solar cell is ignored assuming an ideal antireflective layer is coated, as well as the reflection from the back and the sides of the device.

5.3 Results and Discussion

5.3.1 Simulation of reference solar cell

The structure parameters of the reference solar cell from the literature[50] are given in **Table 5.1**. The layers from the buffer to the cap are grown by low-pressure MOVPE in an Aixtron planetary reactor. This structure incorporates a $Ga_{0.51}In_{0.49}P$ window layer over the front of the p-GaAs emitter and a $Ga_{0.51}In_{0.49}P$ BSF layer beneath the n-GaAs base layer. The solar cell based on this multilayer heterostructure was reported with external quantum efficiency (EQE) higher than 94 % over the wavelength ranging from 600 nm to 900 nm and a power conversion efficiency of 23.3 %.

Table 5.1 Multilayer heterostructure of the reference solar cell[50]

Layer	**Material**	**Thickness**	**Doping**
ARC	MgF_2/TiO_2		
Cap	GaAs	500 nm	p= 3×10^{18} cm^{-3}
Window	GaInP	30 nm	p= 3×10^{18} cm^{-3}
Emitter	GaAs	500 nm	p= 5×10^{18} cm^{-3}
Base	GaAs	3 μm	n= 2×10^{17} cm^{-3}
Back Surface Field	GaInP	250 nm	n= 3.5×10^{18} cm^{-3}
Buffer	GaAs	200 nm	n= 1×10^{18} cm^{-3}
Substrate	GaAs	350 μm	n= 3×10^{18} cm^{-3}

The electrical and spectral response characteristics of this solar cell are simulated in this study. The calculated results of illuminated J-V and EQE are shown and compared with experimental data in **Figure 5.2** and **Figure 5.3**, respectively. The results from the simulation are in good agreement with the measured data, which validates the models and material properties adopted in the simulation. The simulated electrical parameters are: short circuit current density (Jsc) = 28.7 mA/cm^2, open circuit voltage (Voc) = 1.010 V, fill factor (FF) = 84.0 %, efficiency (η) = 24.3 %, while the measurements are: Jsc = 26.7 mA/cm^2, Voc = 1.035 V, FF = 84.3 %, η = 23.3 %. The simulation overestimates the short circuit current and efficiency but underestimates the open circuit voltage and fill factor. The discrepancy may be attributed to the resistive losses and the surface recombination which are not precisely captured in the model. The simulation also presents a quantum efficiency slightly higher at the range of 650-850 nm but lower at the range of 350-650 nm than the experimental data. The inaccuracy of the optical parameters used in the simulation is expected to be the cause of this difference.

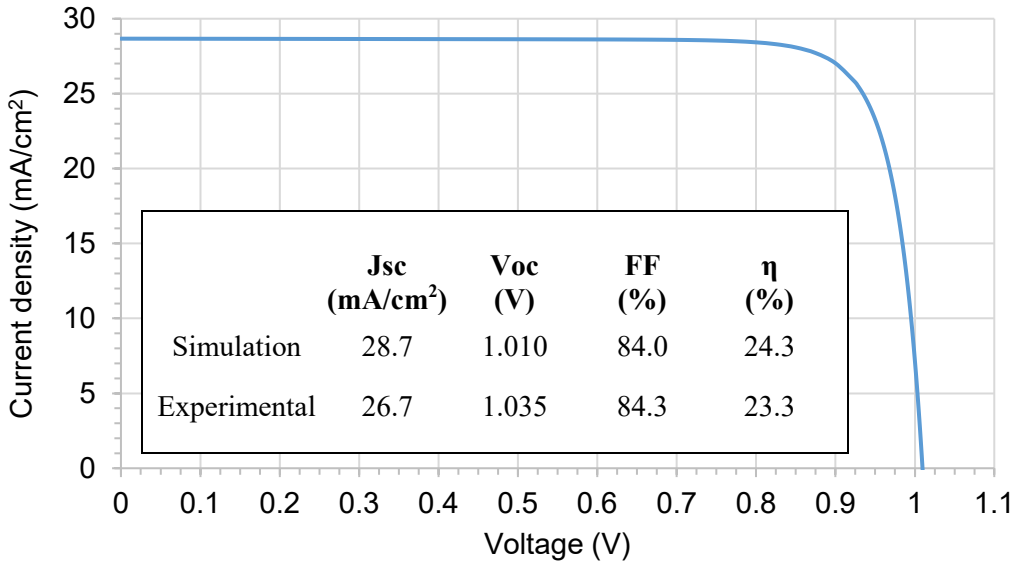

	Jsc (mA/cm²)	Voc (V)	FF (%)	η (%)
Simulation	28.7	1.010	84.0	24.3
Experimental	26.7	1.035	84.3	23.3

Figure 5.1 Simulated J-V curve for the GaAs-based single junction solar cell
The insert compares the simulated electrical characteristics with the reported data[50]

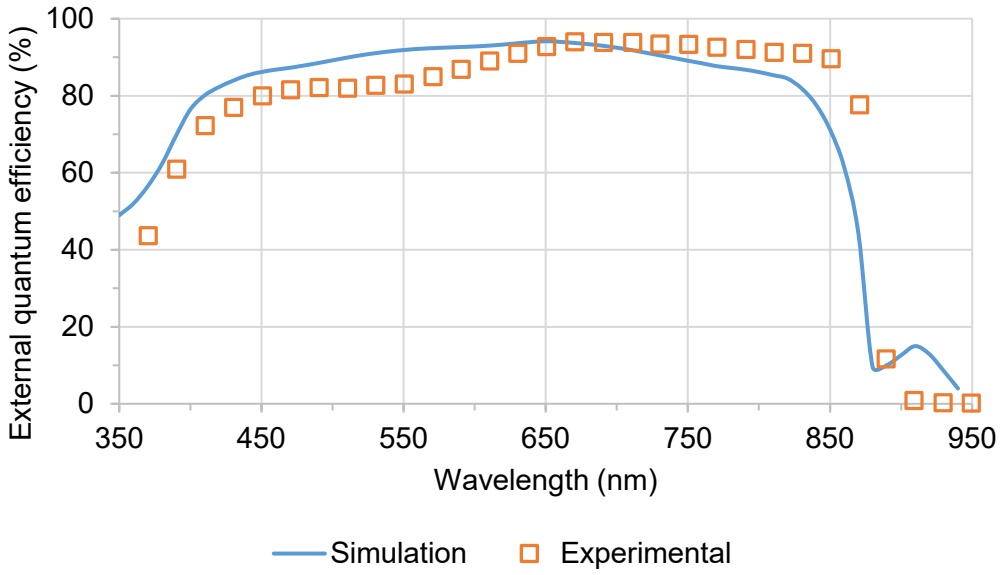

Figure 5.2 Simulated and experimental[50] external quantum efficiency for the GaAs-based single junction solar cell

5.3.2 Parametric study

Based on the reference structure, we further carried out a series of single variable parametric studies to determine sensitive variables affecting device efficiency and an optimal configuration for reactor modeling. The thickness of one layer is varied while the others are fixed constant at the reference values. The efficiency increases as the thickness of the window layer decreases, but the removal of this layer entirely leads to an extremely low efficiency. It confirms the essential role of the wide-bandgap window layer in passivating the emitter and reducing the surface recombination. The window layer needs to be thin to allow more light to pass through and be absorbed in the GaAs layer. The thickness of the window layer is also associated with the sheet resistance.[106] The overall optimization of this layer involves the design of the front grid and may require simulations at higher dimension, which is beyond the scope of this present study. The parametric sweep of the emitter thickness predicts that the optimal thickness of this layer is 300 nm which is smaller than the 500 nm presented in the literature.

Tuning the thickness of the base and the BSF layers around the reference value results in some improvement but the discrepancy is not as significant as the one caused by the variations of the front layers. From the simulation it is also found that the inclusion of the buffer layer and the substrate in the model does not appreciably affect the efficiency. The generation rates are decreased and equal to the recombination rates at the depth of the substrate, indicating the carrier generated in this region cannot be collected and contribute

to the current. Therefore, in the following studies only the layers from the BSF to the window were taken into account to save computational time.

Because the previous results show the efficiency is sensitive to the thickness of the front layers and the structure parameters used in the reference are not optimal, we further examined the variation of conversion efficiency as both the window and the emitter thicknesses are varied around their reference values. The results are plotted in **Figure 5.3**.

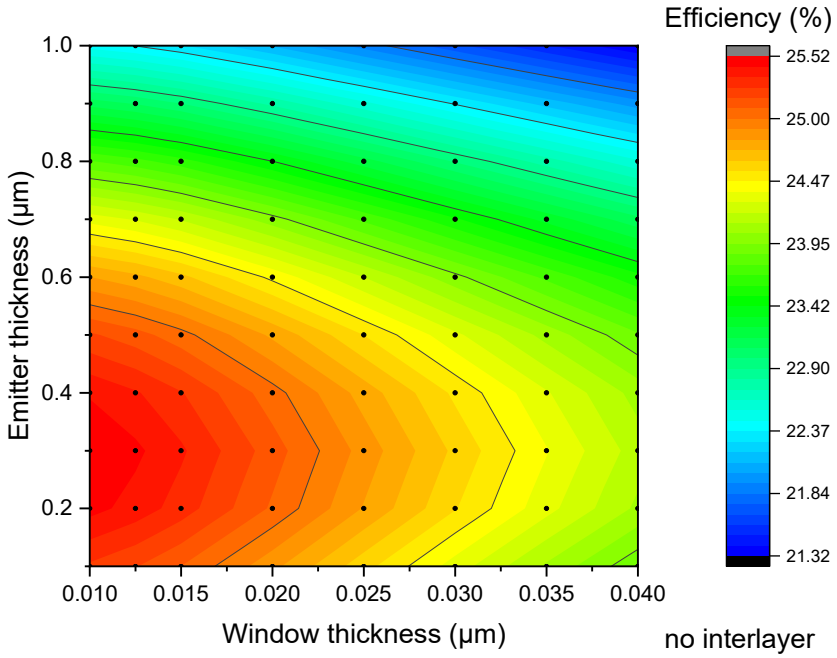

Figure 5.3 Contour of solar cell efficiency as a function of window thickness and emitter thickness

The trend agrees with the result from the single variable study. Over the range of interest, the optimal efficiency is achievable if the thickness of the window layer is tuned

to the lower bound (10 nm) and the thickness of the emitter is adjusted to 300 nm. The electrical parameters of the solar cell updated with this new set of structure parameters are: Jsc = 30.0 mA/cm^2, Voc = 1.015 V, FF = 83.9 %, η = 25.5 %.

5.3.3 Influence of interfacial abruptness

To investigate the impact of the heterointerface abruptness on the device performance, we simulated the J-V characteristics of solar cells with a compositionally graded region at the GaInP-GaAs heterojunction. An interlayer with composition linearly graded from $Ga_{0.51}In_{0.49}P$ to GaAs is sandwiched between the window and the emitter to approximate the non-abrupt heterointerface which could arise in this epitaxial processes from the cross-diffusion of reactants between growth zones. The material of this extra layer can be denoted as $(GaAs)_z(Ga_{0.51}In_{0.49}P)_{1-z}$, which restricts the quaternary interlayer lattice-matched to GaAs. The composition z is changed from 0 to 1 along the depth. The quaternary alloy can also be denoted as $Ga_xIn_{1-x}As_yP_{1-y}$ (x: 0.51 → 1, y: 0 → 1), but x and y in this notation are implicitly related by the lattice-matching condition. Based on the Vegard's law and provided the lattice parameters of III-V binaries, $x = \frac{0.4050-0.1893y}{0.4050+0.0132y}$ for $0 \leq y \leq 1$.[107] The layer will tend to the lattice matched condition due to the thermodynamic effect referred to as lattice-latching or lattice-pulling.[108,109]

From the previous study, we know that the efficiency is less affected by the substrate. Although we have not considered the substrate removal and reuse techniques in our work yet, for the ease of solar cell simulation, we exclude the buffer layer and the

substrate in the following simulations. The previous parametric study of window layer shows that the efficiency monotonically increases as the thickness of the window layer decreases. Hence, we selected a window layer with thickness of 10 nm, thinner than the corresponding layer in the reference structure. Although thinner layer might bring higher efficiency, the increasing difficulty of fabrication and the decreasing conductivity in the front layer make a thinner window layer less practical. The thicknesses of the interlayer and the emitter are two major variables in this study. **Table 5.2** lists the structure information including the thickness, doping, and composition of each layer.

Table 5.2 Multilayer heterostructure with graded interlayer at window-emitter heterojunction

Layer	**Material/Composition**	**Thickness**	**Doping**
Window	$Ga_{0.51}In_{0.49}P$	0-30 nm	p= 3×10^{18} cm^{-3}
Interlayer	$(GaAs)_z(Ga_{0.51}In_{0.49}P)_{1-z}$ z: 0→1	0-30 nm	p= 3×10^{18} cm^{-3}
Emitter	GaAs	0-1 μm	p= 5×10^{18} cm^{-3}
Base	GaAs	3 μm	n= 2×10^{17} cm^{-3}
Back Surface Field	$Ga_{0.51}In_{0.49}P$	250 nm	n= 3.5×10^{18} cm^{-3}

Figure 5.4 shows the solar cell efficiency as a function of the emitter thickness and the interlayer thickness while the thickness of the window layer is fixed at 10 nm. Due to the lack of reliable optical parameters of $Ga_xIn_{1-x}As_yP_{1-y}$, two limiting cases in which the

refractive index of composition-graded interlayer is approximated by that of GaAs and $Ga_{0.51}In_{0.49}P$ are calculated respectively to account for the influence of refractive index on the efficiency. The results are shown in **Figures 5.4(a**) and **(b)**. From the profile and magnitude of the efficiency, it is clearly seen that the discrepancy caused by the selection of the refractive index is marginal, which justifies the simulation without using refractive index and extinction coefficient of $Ga_xIn_{1-x}As_yP_{1-y}$ from interpolation.

As is shown in **Figure 5.4**, the efficiency is reduced as the interlayer becomes thicker. The optimal efficiency is achieved when the thickness of the graded interlayer is minimized and the thickness of the emitter is about 300 nm. According to our previous growth study, the thickness of the transition region over the film can be controlled to less than 5 nm with the separation zones operated under appropriate conditions. The figure here shows the impact of an interlayer thinner than 5 nm on the efficiency is negligible while the thickness of emitter is about 300 nm. The result from this study demonstrates the importance of precise interface and thickness control during the multilayer growth and relates the performance of the epitaxial growth process with the performance of the final device.

(a)

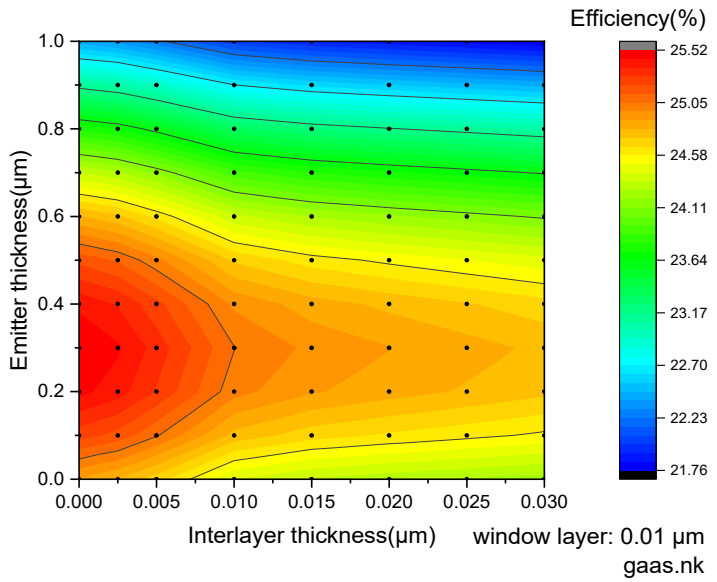

(b)

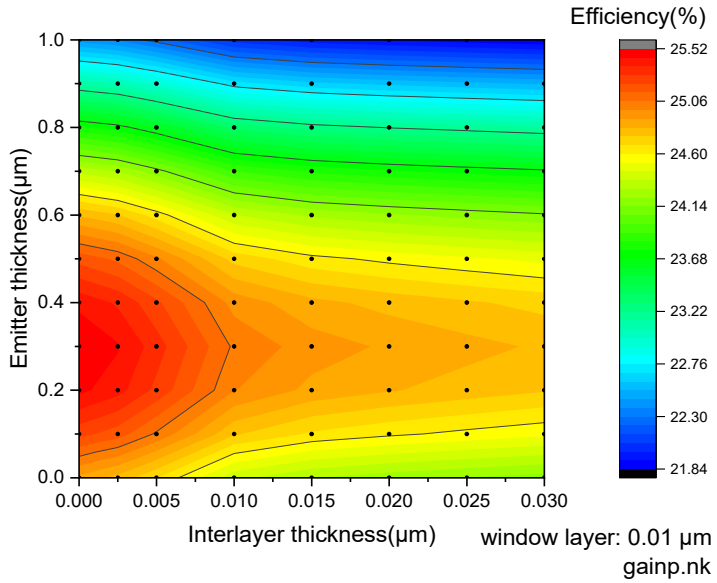

Figure 5.4 Contour of solar cell efficiency as a function of interlayer thickness and emitter thickness

5.4 Conclusions

In conclusion, we developed the approach of device modeling for the quantification of III-V multilayer heterostructure quality in term of solar cell efficiency for the development of continuous HVPE process. A high-efficiency GaAs-based solar cell that is suitable to be manufactured through this process was evaluated through the numerical simulation. The dependence of solar cell efficiency on the interfacial abruptness was investigated. It is found that the compositionally graded GaInAsP extra interlayer between GaInP-window and GaAs-emitter negatively affects the conversion efficiency of GaAs single junction solar cell. The solar cell efficiency decreases as the thickness of this interlayer increases. This result further proves that the thickness of the multilayer structure must be precisely controlled to attain an abrupt interface in order to guarantee the desirable device performance besides the concerns of defects and dislocations introduced into interlayers thicker than critical thickness during epitaxial growth. The result of this study confirms the effectiveness of our continuous HVPE process in the growth of heterostructures. The methods developed in this work can be further applied to design more advanced III-V solar cell structures and to guide the optimization of growth system.

5.5 Appendix

Table 5.3 Model explanation adapted from Atlas manual[103]

Model used with "MODELS" statement			
Category	**Model**	**Syntax in Atlas**	**Notes**
Carrier statistics models	Fermi-Dirac	FERMI	Reduced carrier concentrations in heavily doped regions
	Bandgap narrowing	BGN	Bandgap narrowing model in Slotboom formulation.[110] Update the parameters of BGN.E, BGN.N, and BGN.C in the MATERIAL statement. Important in heavily doped regions. BGN effects are important only for p-GaAs regions and Blaze by default uses values from a doping versus bandgap narrowing table
	Fermi statistics for the calculation of the intrinsic concentration	NI.FERMI	Includes the effects of Fermi statistics into the calculation of the intrinsic concentration in expressions for SRH recombination
Mobility model	Concentration dependent mobility	CONMOB	Concentration dependent mobility model be used for gallium arsenide. This model is a doping versus mobility table valid for 300K only

Table 5.3 continued

Recombination models	Shockley-Read-Hall recombination	SRH	SRH recombination with fixed lifetimes
	Band-band recombination	OPTR	Essential for direct materials
	Auger recombination	AUGER	Direct transition of three carriers
Band parameter model		CUBIC35	Material dependent band parameter model for cubic III-V semiconductors
Model used with other statement			
Category	**Statement**	**Syntax in Atlas**	**Notes**
Mobility model	MOBILITY	N.SOTOODEH P.SOTOODEH	Sotoodeh's low-field mobility model of electrons or holes for $Ga_xIn_{1-x}As_yP_{1-y}$ system[111]
Recombination model	INTERFACE	S.N S.P	Surface recombination

6. CONCLUSIONS

6.1 Contributions

The hydride vapor phase epitaxial growth of III-V multilayer heterostructures has regained research attention in recent years due to the growing interest in the manufacture of low-cost III-V photovoltaics and the inherent advantages of HVPE including rapid growth rates and low precursor costs. However, the high growth rates and the latency of gas switching associated with the in-situ generation of group III precursors in the traditional HVPE process impose difficulties of achieving well-defined and abrupt interfaces using this approach. Taking this challenge as an opportunity for process innovation, this work is motivated to design a new HVPE growth system in order to translate the advantages of hydride VPE method into the rapid growth of III-V compounds and overcome the technical challenge in the precise control of heterojunction formation by HVPE through process design.

The studies carried out to achieve this goal are summarized below.

Proposal of continuous HVPE growth system

A fully continuous moving belt HVPE deposition system that targets the low-cost growth of III-V heterostructures is presented. This proposed deposition system comprises multiple deposition chambers and interconnecting separation zones. Independent growth condition is established at steady state in each deposition zone to avoid the “latency” effect of gas switching on the formation of sharp interface. The placement of separation zone

decouples the growth environment in different deposition zones and quenches the growth automatically to control the interfacial composition abruptness. This continuous HVPE growth system further includes a moveable belt configured to continuously convey substrates through the linear cluster of the deposition and separation zones and a gas delivery assembly configured to deliver reactant gas mixtures to the growth system for deposition on the substrate via HVPE. We are expecting this design can aid the high throughput production of III-V multilayer heterostructures with controlled quality and potentially promote the widespread adoption of III-V photovoltaics in terrestrial applications.

Model development for the continuous HVPE growth of III-V multilayer heterostructures

The methodology to computational design of a continuous HVPE reactor is developed. Based on the general framework of CFD modeling of CVD reactors, this work updates the moving mesh feature to model the dynamics of substrate movement during continuous growth and presents a semi-empirical kinetic model for HVPE growth of GaAs semiconductor and related alloys to relate the growth rate with gas-phase conditions. Incorporating the kinetic model, the resultant reactor model establishes the relationship between the film properties and the growth conditions which is strongly dependent on the reactor geometry, therefore can be served as a powerful tool aiding the reactor and process design.

Application of the III-V HVPE modeling tool

The model formulated previously is adopted to investigate the transport phenomena and the epilayer deposition in the growth system. The effect of moving substrate on the transport phenomena in the reactor is studied through a time-dependent modeling of HVPE growth of GaInP-GaAs bilayer at a relatively long-time duration. It is found that the variations of gas-phase concentrations at several representative sampled locations in the reactor show periodic characteristics while the deposition is occurring on moving substrates. This periodicity is used to simplify the solution of the model. The modeling tool is applied to investigate the effect of the design variables of the separation zone on the abruptness of the interfacial composition transition in heterostructures. It is shown that a sharp interface can be produced by decreasing the height of the separation zone even without a gas curtain. The model is further used to simulate the growth of a multilayer structure in solar cells. The feasibility of continuous growth in the proposed continuous system is verified.

Integration of solar cell simulation

To measure the performance of the process in term of device efficiency and to optimize the process for the growth of high-efficiency solar cell structures, we further incorporated the solar cell simulation into the modeling framework for process design. The electrical and optical characteristics of a GaAs-based single junction solar cell structure reported with high efficiency was simulated. The simulated characteristics of the reference solar cell are in good agreement with the measurements. Parametric studies were carried out to evaluate the dependence of the efficiency on the device structure parameters and

present an improved solar cell structure for epitaxial growth. The influence of interfacial composition abruptness at the GaInP-GaAs heterojunction on the efficiency of this solar cell was systematically investigated. It is found that the compositionally graded GaInAsP extra interlayer between GaInP-window and GaAs-emitter negatively affects the conversion efficiency of GaAs single junction solar cell. The solar cell efficiency is reduced as the thickness of this interlayer increases. The result of this study confirms the effectiveness of our continuous HVPE process in the growth of heterostructures. The methods developed in this work can be further applied to design more advanced III-V solar cell structures and to guide the optimization of growth system.

6.2 Future Work

Continuation and refinement of the proposed growth system

The present work concentrates on the development of the core part in the continuous growth system: the deposition and separation zones. However, in an actual growth system, other zones and auxiliary subsystems also strongly affect the overall process performance. For the fabrication of high quality materials using HVPE, the operating conditions in the source and mixing zones play essential roles to guarantee the well-controlled deposition in the downstream deposition zones. Moreover, the source and mixing zones in the traditional batch process no longer suffice the production demand and fit the physical architecture of the present large-scale continuous growth system, therefore are required to be properly re-designed. The modeling methods developed in this work can

be applied to predict the performance of prospective configurations and optimize the geometrical and operating parameters of these zones.

To meet the material specifications and guarantee the heterostructure interface quality in a continuous growth system, it is necessary to include real-time in situ sensors and integrate closed-loop feedback control to precisely control the film thickness and composition, in addition to the measures such as careful design of the deposition and separation zones and appropriate operating conditions. There are published studies of the process control of HVPE process. With the development of a fully automated continuous HVPE reactor system, the work in the implementation of control configuration for this growing environment should be carried out.

It is also recommended that the development of the physical equipment can be undertaken in parallel with the refinement of growth system using computational modeling. The experimental data from the physical growth tool can be used to refine estimates of the model's parameters and verify the model predictions. The model and experiment can complement each other and effectively facilitate the design of a novel and impactful growth system.

REFERENCES

1. Ekins-Daukes NJ. III-V Solar Cells. In: Conibeer G, Willoughby A, eds. *Solar Cell Materials: Developing Technologies*. John Wiley & Sons, Ltd; 2014:113-143.

2. Green MA, Hishikawa Y, Dunlop ED, Levi DH, Hohl-Ebinger J, Ho-Baillie AWY. Solar cell efficiency tables (version 51). *Prog Photovolt Res Appl*. 2018;26(1):3-12.

3. Vurgaftman I, Meyer JR, Ram-Mohan LR. Band parameters for III–V compound semiconductors and their alloys. *Journal of Applied Physics*. 2001;89(11):5815-5875.

4. Hamaguchi C. Energy Band Structures of Semiconductors. In: Hamaguchi C, ed. *Basic Semiconductor Physics*. Berlin, Heidelberg: Springer Berlin Heidelberg; 2001:1-23.

5. Kuech TF. III-V compound semiconductors: growth and structures. *Progress in Crystal Growth and Characterization of Materials*. 2016;62(2):352-370.

6. Kuech TF, Mawst LJ, Brown AS. Mixed semiconductor alloys for optical devices. *Annu Rev Chem Biomol Eng*. 2013;4(1):187-209.

7. Bailey S, Raffaelle R. Space Solar Cells and Arrays. In: *Handbook of Photovoltaic Science and Engineering*. Wiley-Blackwell; 2011:365-401.

8. Andreev VM. GaAs and High-Efficiency Space Cells. In: Kalogirou SA, ed. *McEvoy's Handbook of Photovoltaics (Third Edition)*. Academic Press; 2018:421-438.

9. Cotal H, Fetzer C, Boisvert J, et al. III–V multijunction solar cells for concentrating photovoltaics. *Energy Environ Sci*. 2009;2(2):174-192.

10. Alferov ZI, Andreev VM, Rumyantsev VD. III-V Solar Cells and Concentrator Arrays. In: *High-Efficient Low-Cost Photovoltaics*. Springer Series in Optical Sciences. Springer, Berlin, Heidelberg; 2009:101-141.

11. Philipps SP, Dimroth F, Bett AW. High-Efficiency III–V Multijunction Solar Cells. In: Kalogirou SA, ed. *McEvoy's Handbook of Photovoltaics (Third Edition)*. Academic Press; 2018:439-472.

12. Apostoleris H, Stefancich M, Chiesa M. High-Efficiency Solar Cells. In: *Concentrating Photovoltaics (CPV): The Path Ahead*. Green Energy and Technology. Springer, Cham; 2018:19-31.

13. Bobela DC, Gedvilas L, Woodhouse M, Horowitz KAW, Basore PA. Economic competitiveness of III–V on silicon tandem one-sun photovoltaic solar modules in favorable future scenarios. *Prog Photovolt: Res Appl*. 2017;25(1):41-48.

14. Ward JS, Remo T, Horowitz K, et al. Techno-economic analysis of three different substrate removal and reuse strategies for III-V solar cells. *Prog Photovolt: Res Appl*. 2016;24(9):1284-1292.

15. Capper P, Irvine S, Joyce T. Epitaxial Crystal Growth: Methods and Materials. In: *Springer Handbook of Electronic and Photonic Materials*. Springer Handbooks. Springer, Cham; 2017:1-1.

16. Woodhouse M, Goodrich A. A manufacturing cost analysis relevant to single- and dual-junction photovoltaic cells fabricated with III-Vs and III-Vs grown on Czochralski silicon. NREL/PR-6A20-60126. September 30, 2013.

17. Choi W, Kim CZ, Kim CS, et al. A repeatable epitaxial lift-off process from a single GaAs substrate for low-cost and high-efficiency III-V solar cells. *Advanced Energy Materials*. 2014;4(16):1400589.

18. Cheng C-W, Shiu K-T, Li N, Han S-J, Shi L, Sadana DK. Epitaxial lift-off process for gallium arsenide substrate reuse and flexible electronics. *Nature Communications*. 2013;4:1577.

19. Mauk MG. Liquid-Phase Epitaxy. In: Kuech TF, ed. *Handbook of Crystal Growth (Second Edition)*. Boston: North-Holland; 2015:225-316.

20. Woodall JM, Hovel HJ. High-efficiency $Ga_{1-x}Al_xAs$–GaAs solar cells. *Appl Phys Lett*. 1972;21(8):379-381.

21. Capper P, Mauk M. *Liquid Phase Epitaxy of Electronic, Optical and Optoelectronic Materials*. John Wiley & Sons; 2007.

22. Knodle WS, Chow R. Molecular Beam Epitaxy: Equipment and Practice. In: Seshan K, ed. *Handbook of Thin Film Deposition Processes and Techniques (Second Edition)*. Norwich, NY: William Andrew Publishing; 2001:381-461.

23. Greenaway AL, Boucher JW, Oener SZ, Funch CJ, Boettcher SW. Low-cost approaches to III–V semiconductor growth for photovoltaic applications. *ACS Energy Lett*. 2017;2(10):2270-2282.

24. Simon J, Young D, Ptak A. Low-cost III-V solar cells grown by hydride vapor-phase epitaxy. In: *2014 IEEE 40th Photovoltaic Specialist Conference (PVSC)*. Denver, CO, USA; 2014:0538-0541.

25. J. Ritenour A, W. Boucher J, DeLancey R, L. Greenaway A, Aloni S, W. Boettcher S. Doping and electronic properties of GaAs grown by close-spaced vapor transport from powder sources for scalable III–V photovoltaics. *Energy & Environmental Science*. 2015;8(1):278-285.

26. Kapadia R, Yu Z, Wang H-HH, et al. A direct thin-film path towards low-cost large-area III-V photovoltaics. *Scientific Reports*. 2013;3:2275.

27. Tietjen JJ, Amick JA. The preparation and properties of vapor-deposited epitaxial $GaAs_{1-x}P_x$ using arsine and phosphine. *J Electrochem Soc*. 1966;113(7):724-728.

28. Lourdudoss S, Kjebon O. Hydride vapor phase epitaxy revisited. *IEEE Journal of Selected Topics in Quantum Electronics*. 1997;3(3):749-767.

29. Gil E, André Y, Cadoret R, Trassoudaine A. Hydride Vapor Phase Epitaxy for Current III–V and Nitride Semiconductor Compound Issues. In: Kuech TF, ed. *Handbook of Crystal Growth (Second Edition)*. Boston: North-Holland; 2015:51-93.

30. Grüter K, Deschler M, Jürgensen H, Beccard R, Balk P. Deposition of high quality GaAs films at fast rates in the LP-CVD system. *Journal of Crystal Growth*. 1989;94(3):607-612.

31. Susa N, Yamauchi Y, Kanbe H. Continuous growth of high purity InP/InGaAs on InP substrate by vapor phase epitaxy. *Jpn J Appl Phys*. 1981;20(4):L253.

32. Nishibe T, Iwamoto M. Hydride VPE growth technique for InP/GaInAsP system. *Journal of Crystal Growth*. 1989;94(3):588-596.

33. Olsen GH. Vapor-Phase Epitaxy of Group III-V Compound Optoelectronic Devices. In: *Integrated Circuits: Chemical and Physical Processing*. Vol 290. ACS Symposium Series. American Chemical Society; 1985:221-240.

34. Schulte KL, Rance WL, Reedy RC, Ptak AJ, Young DL, Kuech TF. Controlled formation of GaAs pn junctions during hydride vapor phase epitaxy of GaAs. *Journal of Crystal Growth*. 2012;352(1):253-257.

35. Schulte KL, Garrod TJ, Wan Kim T, et al. Metalorganic vapor phase growth of quantum well structures on thick metamorphic buffer layers grown by hydride vapor phase epitaxy. *Journal of Crystal Growth*. 2013;370:293-298.

36. Schulte KL, Zutter BT, Wood AW, Babcock SE, Kuech TF. Design and characterization of thick $In_xGa_{1-x}As$ metamorphic buffer layers grown by hydride vapor phase epitaxy. *Semicond Sci Technol*. 2014;29(3):035013.

37. Tsvetkov DV, Nikolaev AE, Dmitriev VA. Apparatus for epitaxially growing semiconductor device structures with submicron group III nitride layer utilizing HVPE. US6706119B2. March 16, 2004.

38. Armour E, Quinn WE, Sferlazzo P. Continuous feed chemical vapor deposition system. US20100310769A1. December 9, 2010.

39. Young DL, Ptak AJ, Kuech TF, Schulte K, Simon JD. High throughput semiconductor deposition system. US9824890B2. November 21, 2017.

40. Simon J, Schulte KL, Young DL, Haegel NM, Ptak AJ. GaAs solar cells grown by hydride vapor-phase epitaxy and the development of GaInP cladding layers. *IEEE Journal of Photovoltaics*. 2016;6(1):191-195.

41. Jain N, Simon J, Schulte KL, et al. InGaAsP solar cells grown by hydride vapor phase epitaxy. In: *2016 IEEE 43rd Photovoltaic Specialists Conference (PVSC)*. Portland, OR, USA; 2016:1090-1094.

42. Simon J, Schulte KL, Jain N, et al. Upright and Inverted Single-Junction GaAs Solar Cells Grown by Hydride Vapor Phase Epitaxy. *IEEE Journal of Photovoltaics*. 2017;7(1):157-161.

43. Schulte KL, Simon J, Mangum J, et al. Development of GaInP solar cells grown by hydride vapor phase epitaxy. *IEEE Journal of Photovoltaics*. 2017;7(4):1153-1158.

44. Schulte KL, Simon J, Ptak AJ. Multijunction $Ga_{0.5}In_{0.5}P$/GaAs solar cells grown by dynamic hydride vapor phase epitaxy. *Progress in Photovoltaics: Research and Applications*. 2018:1-7.

45. Young DL, Ptak AJ, Kuech TF, Schulte K, Simon JD. High throughput semiconductor deposition system. US20150325430 A1. November 12, 2015.

46. Yao M, Rawlings JB, Kuech TF. Modeling of transport and reaction in a novel hydride vapor phase epitaxy system. October 2017.

47. Yao M, Rawlings JB, Kuech TF. Intensification of the hydride vapor phase epitaxy manufacturing process for solar devices. November 2017.

48. Pistor P, Mainz R, Heinemann MD, Unold T, Scheer R. *In Situ* Real-Time Characterization of Thin-Film Growth. In: Abou-Ras D, Kirchartz T, Rau U, eds. *Advanced Characterization Techniques for Thin Film Solar Cells*. Weinheim, Germany: Wiley-VCH Verlag GmbH & Co. KGaA; 2016:441-467.

49. Yan X-T, Xu Y. *Chemical Vapour Deposition: An Integrated Engineering Design for Advanced Materials*. London: Springer-Verlag; 2010.

50. Bett AW, Dimroth F, Stollwerck G, Sulima OV. III-V compounds for solar cell applications. *Appl Phys A*. 1999;69(2):119-129.

51. Galiana B, Rey-Stolle I, Baudrit M, García I, Algora C. A comparative study of BSF layers for GaAs-based single-junction or multijunction concentrator solar cells. *Semicond Sci Technol*. 2006;21(10):1387.

52. Schulte KL, Simon J, Young DL, Ptak AJ. Modeling of gas curtains in a dual chamber hydride vapor phase epitaxial photovoltaic growth reactor. In: *2015 IEEE 42nd Photovoltaic Specialist Conference (PVSC)*. ; 2015:1-5.

53. Mitrovic B, Gurary A, Quinn W. Process conditions optimization for the maximum deposition rate and uniformity in vertical rotating disc MOCVD reactors based on CFD modeling. *Journal of Crystal Growth*. 2007;303(1):323-329.

54. Jensen KF, Fotiadis DI, Mountziaris TJ. Detailed models of the MOVPE process. *Journal of Crystal Growth*. 1991;107(1):1-11.

55. Fotiadis DI, Kieda S, Jensen KF. Transport phenomena in vertical reactors for metalorganic vapor phase epitaxy: I. Effects of heat transfer characteristics, reactor geometry, and operating conditions. *Journal of Crystal Growth*. 1990;102(3):441-470.

56. Ouazzani J, Rosenberger F. Three-dimensional modelling of horizontal chemical vapor deposition: I. MOCVD at atmospheric pressure. *Journal of Crystal Growth*. 1990;100(3):545-576.

57. Salinger AG, Shadid JN, A. Hutchinson S, Hennigan GL, Devine KD, Moffat HK. Analysis of gallium arsenide deposition in a horizontal chemical vapor deposition reactor using massively parallel computations. *Journal of Crystal Growth*. 1999;203(4):516-533.

58. Ingle NK, Theodoropoulos C, Mountziaris TJ, Wexler RM, Smith FTJ. Reaction kinetics and transport phenomena underlying the low-pressure metalorganic chemical vapor deposition of GaAs. *Journal of Crystal Growth*. 1996;167(3):543-556.

59. Cadoret R, Cadoret M. A theoretical treatment of GaAs growth by vapour phase transport for {001} orientation. *Journal of Crystal Growth*. 1975;31:142-146.

60. Cadoret R, Hollan L, Loyau JB, Oberlin M, Oberlin A. GaAs growth by vapour phase transport. *Journal of Crystal Growth*. 1975;29(2):187-194.

61. Korec J, Heyen M. Modeling of chemical vapor deposition: II. Gas phase epitaxy of (100) GaAs. *Journal of Crystal Growth*. 1982;60(2):297-306.

62. Korec J, Heyen M. Modeling of chemical vapor deposition: I. General considerations. *Journal of Crystal Growth*. 1982;60(2):286-296.

63. Seifert W, Schwetlick S, Reinhold J, Butter E. A quantum chemical study of chlorine desorption by hydrogen in the VPE of GaAs. *Journal of Crystal Growth*. 1984;66(2):333-337.

64. Shaw DW. Epitaxial GaAs kinetic studies: {001} orientation. *J Electrochem Soc*. 1970;117(5):683-687.

65. Hong JC, Lee HH. Epitaxial growth rate of GaAs: chloride transport process. *J Electrochem Soc*. 1985;132(2):427-432.

66. Schulte KL, Simon J, Jain N, Young DL, Ptak AJ. A kinetic model for GaAs growth by hydride vapor phase epitaxy. In: *2016 IEEE 43rd Photovoltaic Specialists Conference (PVSC)*. ; 2016:1930-1933.

67. Gil-Lafon E, Piffault N, Cadoret R. Kinetic expression and study of the growth rate of mismatched (Ga,In)AsInP structures grown by hydride vapour phase epitaxy. *Journal of Crystal Growth*. 1995;151(1):80-90.

68. Cadoret M, Chaput L, Banvillet H, Porte A, Pariset C, Cadoret R. Kinetic processes in epitaxy of $Ga_xIn_{1-x}As$ on InP(100) by hydride vapour phase epitaxy. *Thin Solid Films*. 1990;192(2):343-350.

69. Gopalakrishnan N, Dhanasekaran R. On the nucleation and composition analysis of $InAs_{1-x}P_x$ during vapour phase epitaxial growth. *Journal of Crystal Growth*. 1996;162(3):113-120.

70. Koukitu A, Seki H. Thermodynamic analysis for InGaAsP epitaxial growth by the chloride-CVD process. *Journal of Crystal Growth*. 1980;49(2):325-333.

71. Gopalakrishnan N, Dhanasekaran R, Lourdudoss S. Compositional analysis on quaternary $Ga_xIn_{1-x}As_yP_{1-y}$ vapour phase epitaxy: a comparison between theory and experiment. *Materials Chemistry and Physics*. 1997;50(1):70-75.

72. Jensen KF, Einset EO, Fotiadis DI. Flow phenomena in chemical vapor deposition of thin films. *Annual Review of Fluid Mechanics*. 1991;23(1):197-232.

73. Kleijn CR. Computational modeling of transport phenomena and detailed chemistry in chemical vapor deposition – a benchmark solution. *Thin Solid Films*. 2000;365(2):294-306.

74. Talalaev R. Transport Phenomena in Vapor Phase Epitaxy Reactors. In: Kuech TF, ed. *Handbook of Crystal Growth (Second Edition)*. Handbook of Crystal Growth. Boston: North-Holland; 2015:909-942.

75. *ANSYS® Fluent®.* ANSYS, Inc.

76. *COMSOL Multiphysics®.* Stockholm, Sweden: COMSOL AB

77. *CFD-ACE+*. ESI Group

78. Dam CEC, Grzegorczyk AP, Hageman PR, Dorsman R, Kleijn CR, Larsen PK. The effect of HVPE reactor geometry on GaN growth rate — experiments versus simulations. *Journal of Crystal Growth*. 2004;271(1):192-199.

79. Kempisty P, Łucznik B, Pastuszka B, et al. CFD and reaction computational analysis of the growth of GaN by HVPE method. *Journal of Crystal Growth*. 2006;296(1):31-42.

80. Dam CEC, Bohnen T, Kleijn CR, Hageman PR, Larsen PK. Scaling up a horizontal HVPE reactor. *Surface and Coatings Technology*. 2007;201(22):8878-8883.

81. Sytniewski ŁJ, Lapkin AA, Stepanov S, Wang WN. CFD optimisation of up-flow vertical HVPE reactor for GaN growth. *Journal of Crystal Growth*. 2008;310(14):3358-3365.

82. Hemmingsson C, Pozina G, Heuken M, Schineller B, Monemar B. Modeling, optimization, and growth of GaN in a vertical halide vapor-phase epitaxy bulk reactor. *Journal of Crystal Growth*. 2008;310(5):906-910.

83. Schulte KL, Simon J, Roy A, et al. Computational fluid dynamics-aided analysis of a hydride vapor phase epitaxy reactor. *Journal of Crystal Growth*. 2016;434:138-147.

84. Kleijn CR. Chemical Vapor Deposition Processes. In: Meyyappan M, ed. *Computational Modeling in Semiconductor Processing*. Boston, MA: Artech House; 1995:97-229.

85. Donea J, Huerta A, Ponthot J-P, Rodríguez-Ferran A. Arbitrary Lagrangian–Eulerian Methods. In: *Encyclopedia of Computational Mechanics*. John Wiley & Sons, Ltd; 2004.

86. Yang K, Hong F, Cheng P. A fully coupled numerical simulation of sessile droplet evaporation using Arbitrary Lagrangian–Eulerian formulation. *International Journal of Heat and Mass Transfer*. 2014;70(Supplement C):409-420.

87. Hansbo P. Generalized Laplacian smoothing of unstructured grids. *Commun Numer Meth Engng*. 1995;11(5):455-464.

88. Field DA. Laplacian smoothing and Delaunay triangulations. *Commun appl numer methods*. 1988;4(6):709-712.

89. Watanabe H. Halogen Transport Epitaxy. In: *Handbook of Crystal Growth*. Vol 3A. Amsterdam: North Holland; 1994:3-41.

90. Ban VS, Gossenberger HF, Tietjen JJ. Influence of deposition temperature on composition and growth rate of $GaAs_xP_{1-x}$ layers. *Journal of Applied Physics*. 1972;43(5):2471-2472.

91. Ban VS. Mass spectrometric and thermodynamics studies of the CVD of some III–V compounds. *Journal of Crystal Growth*. 1972;17(Supplement C):19-30.

92. Schulte KL, Braun A, Simon J, Ptak AJ. High growth rate hydride vapor phase epitaxy at low temperature through use of uncracked hydrides. *Appl Phys Lett*. 2018;112(4):042101.

93. Conrad RW, Hoyt PL, Martin DD. Preparation of epitaxial $Ga_xIn_{1-x}As$. *J Electrochem Soc*. 1967;114(2):164-166.

94. Jacobs K, Simon I, Bugge F, Butter E. A simple method for calculation of the composition of VPE grown $Ga_xIn_{1-x}As$ layers as a function of growth parameters. *Journal of Crystal Growth*. 1984;69(1):155-160.

95. Belouet C. Kinetics of vapour-phase epitaxial growth of $GaAs_{1-x}P_x$. *Journal of Crystal Growth*. 1972;13(Supplement C):342-345.

96. Sigai AG, Nuese CJ, Enstrom RE, Zamerowski T. Vapor growth of $In_{1-x}Ga_xP$ for p-n junction electroluminescence I. material preparation. *J Electrochem Soc*. 1973;120(7):947-955.

97. Middlebrooks SA. *Modelling and control of silicon and germanium thin film chemical vapor deposition* [dissertation]. Wisconsin: University of Wisconsin-Madison; 2001.

98. Cheimarios N, Koronaki ED, Boudouvis AG. Illuminating nonlinear dependence of film deposition rate in a CVD reactor on operating conditions. *Chemical Engineering Journal*. 2012;181-182:516-523.

99. Varshney A. *Optimization and control of multiscale process systems using model reduction: Application to thin-film growth* [dissertation]. Pennsylvania: Pennsylvania State University; 2007.

100. He X, Razeghi M. Investigation of the heteroepitaxial interfaces in the GaInP/GaAs superlattices by high-resolution x-ray diffractions and dynamical simulations. *Journal of Applied Physics*. 1993;73(7):3284-3290.

101. Gorman BP, Norman AG, Yan Y. Atom probe analysis of III-V and Si-based semiconductor photovoltaic structures. *Microscopy and Microanalysis*. 2007;13(6):493-502.

102. Kim K, Nguyen HD, Mho S, Lee J. Enhanced efficiency of GaAs single-junction solar cells with inverted-cone-shaped nanoholes fabricated using anodic aluminum oxide masks. *International Journal of Photoenergy*. 2013;2013:e539765.

103. *Atlas User's Manual (2018)*. Silvaco, Inc.

104. Létay G, Hermle M, Bett AW. Simulating single-junction GaAs solar cells including photon recycling. *Progress in Photovoltaics: Research and Applications*. 2006;14(8):683-696.

105. Plá J, Barrera M, Rubinelli F. The influence of the InGaP window layer on the optical and electrical performance of GaAs solar cells. *Semiconductor Science and Technology*. 2007;22(10):1122-1130.

106. Green MA. *Solar Cells: Operating Principles, Technology, and System Applications*. Prentice-Hall; 1982.

107. Adachi S. III-V Ternary and Quaternary Compounds. In: *Springer Handbook of Electronic and Photonic Materials*. Springer Handbooks. Springer, Cham; 2017:725-741.

108. Stringfellow GB. The importance of lattice mismatch in the growth of $Ga_xIn_{1-x}P$ epitaxial crystals. *Journal of Applied Physics*. 1972;43(8):3455-3460.

109. Wood DM, Zunger A. Composition pinning in epitaxial alloys. *Phys Rev B*. 1988;38(17):12756-12759.

110. Slotboom JW, de Graaff HC. Measurements of bandgap narrowing in Si bipolar transistors. *Solid-State Electronics*. 1976;19(10):857-862.

111. Sotoodeh M, Khalid AH, Rezazadeh AA. Empirical low-field mobility model for III–V compounds applicable in device simulation codes. *Journal of Applied Physics*. 2000;87(6):2890-2900.